Cite as:

Gašper Krivic and Janko Slavič, Single-process 3D-printed bimorph electrothermal soft actuators, International Journal of Mechanical Sciences (2025), https://doi.org/10.1016/j.ijmecsci.2025.110299

Single-Process 3D-Printed Bimorph Electrothermal Soft Actuators

Gašper Krivic[a], Janko Slavič[a,*]

[a] *University of Ljubljana, Faculty of Mechanical Engineering, Aškerčeva 6, Ljubljana, 1000, Slovenia*

Abstract

The manufacturing of bimorph, electrothermal actuators conventionally requires multiple processing steps, which limits design flexibility and customization. Thermoplastic extrusion 3D-printing offers a single-process method for manufacturing complex, multi-material geometries without additional assembly, thereby enhancing the design versatility. While single-process, 3D-printed sensors (e.g., piezoresistive or piezoelectric) have been extensively studied, the development of single-process, 3D-printed actuators remains limited. Key challenges in 3D-printed, thermoplastic actuators include orthotropic, time- and temperature-dependent material behavior, stress relaxation, and single-process design.

This study introduces a novel single-process 3D-printing method, and an analytical model for predicting the time-dependent tip deflection and blocking force of multilayer electrothermal actuators. The actuator is fully 3D-printed and consists of three material layers: a high-coefficient-of-thermal-expansion (CTE) layer, a heater layer, and a low-CTE layer. The pro-

*Corresponding author.
Email address: `janko.slavic@fs.uni-lj.si` (Janko Slavič)

posed analytical model is distinctive in that it incorporates orthotropic, temperature-dependent material properties and accounts for stress-relaxation effects–factors typically neglected in conventional models. It predicts time-dependent tip deflection and blocking force as function of the applied voltage and is experimentally validated using actuators with two distinct material configurations.

The experimental results show close agreement with the model predictions, confirming the accuracy and reliability of the proposed approach. Moreover, the integration of a single-process manufacturing method with the novel, comprehensive analytical framework provides a robust foundation for advancing the development of 3D-printed, electrothermal actuators with improved actuation speed. These findings underscore the potential of scalable, high-performance, electrothermal actuators, manufactured in a single process, for actively controlled shape-morphing structures. This work paves the way for the future integration of actuation functionality into single-process, 3D-printed, smart and responsive devices.
Keywords: 3D printing, electrothermal actuators, modeling, single-process manufacturing, tip deflection, blocking force

---

1. Introduction

Soft actuators are important for advancing next-generation technologies in robotics, biomedicine, and wearable devices due to their flexibility, adaptability, and reconfigurability–attributes that mimic the complex behaviors of living systems [1]. These characteristics enable safe and adaptive interactions with delicate or irregular environments, making soft actuators suitable for applications where rigid systems are ineffective [1, 2]. Despite these advantages, current soft actuator designs often require complex, multi-step manufacturing and rely on simplified analytical models that do not capture key behaviors such as stress relaxation and the temperature-dependent orthotropic properties of 3D-printed materials. Addressing these limitations is required to develop smart, single-process, 3D-printed, shape-morphing structures capable of active and precise responses in real-world settings.

Soft actuators exhibit shape transformations in response to external stimuli such as light [3, 4], electricity [5, 6, 7], magnetic fields [8, 9], pneumatic pressure [10], humidity [11, 12], temperature [13, 14, 15], chemical reactions [16], or combinations of multiple stimuli [17, 18]. Electrical stimulation is among the most promising techniques for practical applications due to its convenience, controllability, and ease of use [19]. Despite their typically low blocking force, electrically driven actuators are very attractive due to their design versatility, lightweight construction, compact size, and the accessibility of electrical power, making them suitable for diverse applications like artificial muscles [20], soft robots [21, 22, 23], soft grippers [24], and metasurfaces [25].

Electrothermal actuators utilize Joule heating, generated by an electrical current passing through a resistive material, to induce a thermal expansion [26, 27, 28]. A typical design features a bimorph structure, with one layer having a high coefficient of thermal expansion (CTE) and another having a low CTE [29]. Resistive heating occurs either in the low-CTE layer or in an additional layer containing an embedded heater. Upon heating, the mismatch in the CTEs between layers causes the actuator to bend towards the low-CTE layer [30]. Electrothermal actuators are advantageous due to their low power consumption, customizable deformation, and high precision, making them well-suited to applications in robotics and flexible devices [31, 32]. In addition to actuation, recent advances have incorporated integrated sensing capabilities into electrothermal actuators. For instance, Wang et al. [33], Pimpin et al. [34], and Liu et al. [35] developed self-sensing electrothermal actuators, however; these actuators are based on multi-process manufacturing techniques.

3D-printing has expanded the possibilities for electrothermal actuators by enabling the manufacture of conductive patterns and complex geometries, allowing for tailored thermal responses and deformations in advanced applications such as soft robots [36, 37, 38] and soft grippers [39, 40, 41]. Thermoplastic extrusion, 3D-printing further transforms electrothermal actuator manufacturing by reducing costs and enabling the production of versatile, multi-material, multifunctional structures across various scales [42]. Moreover, thermoplastic extrusion, 3D-printing facilitates the single-process manufacturing of smart structures [43], including dielectric actuators [44], force sensors [45], accelerometers [46], and active metamaterials [47]. However, current thermoplastic extrusion, 3D-printed, electrothermal actuators still rely on multi-process manufacturing, including pre- or post-processing steps.

Present electrothermal actuators typically utilize a standard copy paper as one material layer due to its low CTE, light weight, and flexibility, combined with shape-memory polymers (SMPs), which can undergo large geometric changes when heated, enabling programmable deformation [48, 49, 50]. However, these actuators require a multi-step manufacturing process that involves preparing the paper as a printing surface, cutting the actuator from it, and performing an additional shape-memory programming step. This programming involves heating the SMP above its glass-transition temperature, stretching to induce internal stresses, cooling under deformation to fix the temporary shape, and finally releasing the constraints [51, 52]. Consequently, such actuators cannot be classified as entirely 3D-printed and cannot be directly integrated into a smart structure.

Several studies have explored thermoplastic extrusion, 3D-printed, electrothermal actuators, demonstrating their capabilities, while requiring multi-process manufacturing techniques. For example, in 2021, Chen and Peng [48] introduced a thermoplastic extrusion, 3D-printed, electrothermal actuator for a starfish-shaped gripper. This actuator demonstrated reversible shape changes over 100 cycles but required printing the SMP onto paper, followed by integrating a graphene sheet as a heating element, adding an additional step to the manufacturing process. In 2022, Duan et al. [49] demonstrated a bilayer electrothermal actuator with reversible deformations, manufactured by the thermoplastic extrusion, 3D-printing of SMP onto paper. This actuator powered a soft crawling robot equipped with asymmetrical, variable-friction feet. That same year, Lee et al. [51] developed an electrothermal actuator composed entirely of SMP. By varying the printing speed, they tuned the SMP's properties and evaluated their effect on the bending performance. Additionally, in 2022, Jian Jiao et al. [53] introduced a stiffness-tunable, shape-locking, electrothermal actuator. After 3D-printing, conventional wires were embedded into the material layers through predesigned holes for heating, adding another processing step. In 2023, Chen and Liao [50] presented a thermoplastic extrusion, 3D-printed, bilayer electrothermal actuator with SMP deposited onto paper. This actuator was used in a lightweight soft robot with four legs, enabling controllable gaits by pairing the legs. In 2024, Chen and Chen [54] manufactured a SMP electrothermal actuator for a soft gripper with four fingers capable of grasping a spherical object. This actuator required multiple sequential processes, including the thermoplastic extrusion, 3D-printing of SMP onto paper, direct ink writing to deposit a conductive polymer matrix composite heater, and laser cutting to release the multilayer structure. Similarly, in 2024, Delbart et al. [52] developed a multi-shape actuator using thermoplastic extrusion, 3D-printing in a single process, with an integrated, electrical self-triggering system. The design incorporated a shape-memory, carbon-black PLA layer embedded within TPU layers of varying thickness to achieve the bending motion; however, the bending cycle could only be reproduced once, unless the shape-memory reprogramming was repeated.

During actuation, multilayer actuators are subjected to shear forces at the layer interfaces, which can lead to delamination over time and reduce actuator longevity [55]. To address this issue, several strategies have been proposed, including the development of single-layer actuators [55], mechanical interlocking of layers [56], and the introduction of a third layer with enhanced bonding. The latter approach shifts the neutral plane toward the critical interface, thereby reducing interfacial stresses and minimizing delamination [57]. For thermoplastic-extrusion 3D-printed electrothermal actuators, strong layer interfaces can be achieved by selecting compatible materials that promote strong interlayer adhesion in multimaterial 3D printing [58, 59]. However, these actuators also exhibit long activation times and high energy consumption due to the low thermal diffusivity and high electrical resistivity of thermoplastics, making them unsuitable for fast, real-time applications such as artificial muscles or soft grippers [60]. To address this, researchers have assisted electrothermal actuation with pneumatic pressure [61] or string mechanisms [62], which complicates the design and limits the integration of such actuators into single-process smart structures. However, single-process 3D-printed electrothermal actuators still hold significant potential for smart shape-morphing structures that actively modulate their shape in response to external loads [63]. Metamaterials with tunable properties, such as stiffness [64], Poisson's ratio [65], and thermal expansion [66], can be actively controlled by electrothermal actuators and integrated into smart structures. For example, the snap-through behavior of the metamaterial presented by Nam et al. [63] can be controlled by electrothermal actuation, as can the geometry of base cells to modulate stiffness [64] or Poisson's ratio [65]. Furthermore, given the design flexibility of thermoplastic extrusion 3D-printing, this approach holds promise for developing lightweight, shape-adaptable, actively controlled smart structures manufactured in a single process.

Analytical models are essential for designing effective and controllable smart structures, achieving high-precision applications, and optimizing actuator performance [67, 68]. However, studies on thermoplastic extrusion, 3D-printed, electrothermal actuators predominantly focus on the manufacturing process and typically report actuator displacement without providing or comparing results with analytical models. The performance of an electrothermal actuator is commonly evaluated based on its tip deflection and blocking force, where the blocking force is defined as the maximum force generated at the actuator's tip when its deflection is fully constrained. While analytical models are critical for predicting these metrics, existing models in the scientific literature typically assume isotropic, temperature-independent material properties. However, thermoplastic extrusion, 3D-printed structures exhibit orthotropic properties with a temperature dependence [69, 70], and the behavior of thermoplastic polymers is further influenced by stress relaxation [71, 72, 73]. Consequently, applying conventional analytical models to thermoplastic extrusion, 3D-printed, electrothermal actuators results in inaccuracies.

The analytical models in the scientific literature are predominantly based on the work of Timoshenko [74], who proposed an analytical model for a bi-metal strip under uniform heating, providing equations to determine the curvature and deflection for specific boundary conditions. In 2010, Du et al. [75] extended Timoshenko's model by developing a multilayer bending model, demonstrating that neglecting the heating layer leads to inaccuracies in the curvature predictions unless the heating layer is extremely thin and compliant. For force analysis, Chu et al. [76] developed an analytical model to predict the tip deflection and blocking force of a bimetallic cantilever actuator. More recently, in 2022, Kim et al. [77] combined these approaches to present analytical models capable of estimating both the tip deflection and the blocking force of multilayer bimorph actuators. Additionally, comprehensive analytical models for bimorph, electrothermal actuators that integrate electrothermal and thermal-mechanical behavior have been proposed by Cao and Dong [68], Tibi et al. [78, 79], and Todd and Huikai Xie [80]. These models relate heating power to temperature rise and subsequently to bending curvature via thermally induced bending. However, they lack predictions for the blocking force and fail to account for the temperature-dependent orthotropic material properties, which are critical for accurately modeling the thermoplastic extrusion, 3D-printed structures.

Traditional manufacturing approaches for electrothermal actuators involve multiple processing steps, increasing complexity, cost, and the risk of cumulative performance errors. In contrast, thermoplastic extrusion 3D-printing enables single-process manufacturing, eliminating post-processing and thereby reducing production time, minimizing error accumulation, and facilitating seamless integration into smart, adaptive systems. Tip deflection is a key performance metric, as it determines the actuator's displacement range–critical for achieving the desired motion in applications such as artificial muscles, soft robotics, and adaptive metamaterials. Inaccurate deflection predictions can result in inadequate or excessive motion, leading to suboptimal performance. Furthermore, the absence of reliable blocking force predictions in existing models affects actuator design by causing over- or under-dimensioning, which compromises efficiency and may introduce safety risks in load-bearing applications. These inaccuracies also hinder integration into smart structures, where consistent and predictable force output is essential.

To overcome these limitations, this study focuses on single-process, 3D-printed, multilayer, electrothermal actuators. It introduces the design principles and the analytical model for predicting the time-dependent tip deflection and blocking force. The fully 3D-printed actuator comprises three material layers: a high-CTE layer, a heater, and a low-CTE layer. The analytical model incorporates orthotropic, temperature-dependent material properties and accounts for the stress-relaxation effects. It accurately predicts the time-dependent tip deflection and blocking force based on the applied voltage and is experimentally validated using actuators with two distinct material configurations.

The manuscript is structured as follows. In Sec. 2, the theoretical background and prior research relevant for the analytical model are presented. The design of the single-process, 3D-printed, bimorph, electrothermal actuator and the proposed analytical model for tip deflection and blocking force are introduced in Sec. 3. In Sec. 4, the 3D-printing for the single-process, bimorph, electrothermal actuator and the experimental methods for tip-deflection and blocking-force measurements are described. In Sec. 5, the results and discussion of the experimental validation of the analytical model are provided, along with a comprehensive sensitivity analysis. Finally, the conclusions are drawn in Sec. 6.

2. Theoretical Background

This section presents the prior knowledge required for the analytical model of the 3D-printed, bimorph, electrothermal actuator introduced in Sec. 3.

For structures with material deposition in a single direction, as shown in Fig. 1, the material properties are assumed to be symmetric across three orthogonal planes, resulting in orthotropic material properties [81]. The

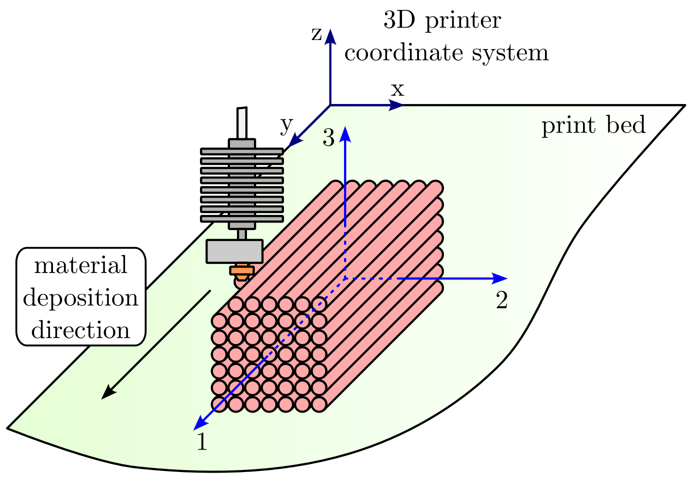

Figure 1: Schematic of a unidirectional 3D-printed structure illustrating its principal material coordinate system: axis 1 is aligned with the print direction, axis 2 lies in-plane and perpendicular to the print direction, and axis 3 is normal to the printed layers, representing orthotropic material behavior.

material properties vary along the three principal axes: the 1st principal axis is aligned with the material-deposition direction, the 2nd is perpendicular to it, and the 3rd is orthogonal to the layers, as shown in Fig. 1.

Fig. 2 shows the three-layer, bimorph, electrothermal actuator. The 1st material layer (M1) has a high CTE, the 2nd material layer (M2) serves as the heater, and the 3rd material layer (M3) has a low CTE. If no voltage is applied to the heater, the actuator remains in its initial state, as shown in Fig. 2a, with a length L, width w, and thickness of each material layer t_i. When a voltage is applied to the heater, Joule heating generates a temperature change $+\Delta T$, causing the material layers to expand. Due to the different CTEs, the material layers with a low CTE are pulled by those with a high CTE, and vice versa, resulting in a new length L^0 and curvature κ_x of the mid-plane,

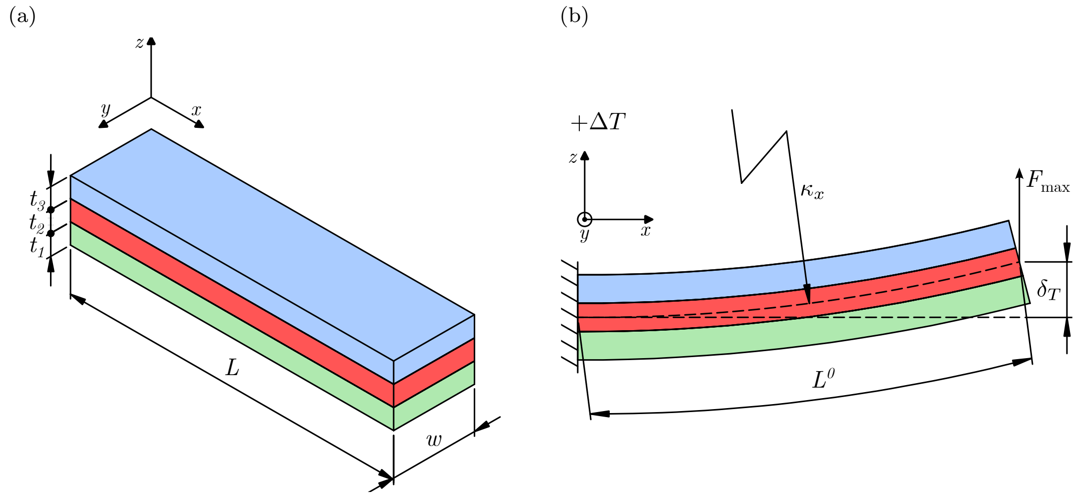

Figure 2: (a) Schematic of the three-layer bimorph actuator in its initial state, with layers arranged from bottom to top as M1 (high CTE), M2 (heater), and M3 (low CTE). (b) Actuated state when a voltage is applied to M2, causing a temperature increase. The resulting thermal expansion mismatch induces a mid-plane curvature κ_x, leading to a tip deflection δ_T and a blocking force $F_{\max}$.

as shown in Fig. 2b. This upward bending of the actuator generates a tip deflection δ_T and a blocking force $F_{\max}$. The analytical modeling of the Joule heating is presented in Sec. 2.1, and the tip deflection and blocking force are discussed in Sec. 2.2.

2.1. Electrothermal Heating

The temperature distribution in a one-dimensional, homogeneous medium is described by the heat equation [82, 83]:

$$\frac{\partial^2 T}{\partial x^2} + \frac{\dot{q}}{k} = \frac{1}{a}\frac{\partial T}{\partial t}, \tag{1}$$

where T is the temperature distribution as a function of the spatial coordinate x and time t: $T(x,t)$, $\dot{q}$ is the rate of energy generation per unit volume, k is the thermal conductivity, and $a = k/\rho/C_p$ is the thermal diffusivity, with ρ and C_p representing the mass density and specific heat at constant pressure, respectively.

In electrothermal heating, thermal energy is generated by converting electrical energy into heat through a resistor, a process known as Joule heating [82]. If the energy generation is uniform throughout the volume V of the resistor, the volumetric generation rate is defined as [84, 85]:

$$\dot{q} = \frac{\dot{E}_g}{V}, \tag{2}$$

where $\dot{E}_g$ is the rate at which thermal energy is generated within the volume of the resistor. Assuming that all the electrical power is converted into thermal energy and that the resistor obeys Ohm's law, the rate of thermal energy generation $\dot{E}_g$ at an applied voltage U is [86]:

$$\dot{E}_g = \frac{U^2}{R}, \tag{3}$$

where R is the electrical resistance of the resistor, defined as [87, 88]:

$$R = \rho_e \frac{l}{A}, \tag{4}$$

with ρ_e representing the electrical resistivity of the material, l the length, and A the cross-sectional area of the resistor. In general, the electrical resistivity of the material is a function of temperature $\rho_e(T)$ [89, 90, 91].

To solve the heat equation (1), the initial and boundary conditions must be specified. If the medium has a uniform temperature T_0 before the conditions change, the initial condition is given as [82]:

$$T(x, 0) = T_0. \tag{5}$$

If the surface of the medium is in contact with a liquid or gas at $x = x_0$ and no radiant heat transfer occurs, the convection boundary condition is applied [82]:

$$-k\frac{\partial T}{\partial x}\bigg|_{x_0} = h[T_\infty - T(0, x_0)], \tag{6}$$

where h is the convection heat-transfer coefficient, and T_∞ is the temperature of the liquid or gas.

For a one-dimensional composite medium, the heat equation (1) is solved separately for each material. At the common surface between the materials 1 and 2 at $x = x_{1,2}$, the boundary conditions of continuity for temperature and heat flow are applied [85]:

$$T_1(x_{1,2}, t) = T_2(x_{1,2}, t), \tag{7}$$

$$-k_1\frac{\partial T_1}{\partial x}\bigg|_{x_{1,2}} = -k_2\frac{\partial T_2}{\partial x}\bigg|_{x_{1,2}}. \tag{8}$$

2.2. Analytical Model of Electrothermal Actuator

Due to the thick material layers of the actuator and its orthotropic material properties, the analytical model for the tip deflection and blocking force of a multilayer, bimorph, electrothermal actuator is based on Classical Lamination Theory (CLT) [92, 93, 94]. To keep the main text concise, a detailed explanation of CLT is provided in Appendix A.

Tip Deflection. For an electrothermal actuator with fixed-free boundary conditions, as shown in Fig. 2b, tip deflection is defined as [76, 77]:

$$\delta_T = \frac{1 - \cos(L^0\,\kappa_x)}{\kappa_x}, \tag{9}$$

where κ_x is the curvature in the x-axis direction (see Fig. 2), and $L^0 = L(1+\varepsilon_x^0)$ is the deformed length at the mid-plane, determined from the initial length of the actuator L and the mid-plane strain in the x-axis direction ε_x^0. The curvature κ_x and the strain ε_x^0 are obtained by solving Eq. (A.15), considering only thermal loads, as no external forces act on the actuator.

Blocking Force. For the actuator with fixed-free boundary conditions, as shown in Fig. 2b, the blocking force is defined as [76, 77]:

$$F_{\max} = \underbrace{\frac{3(E\,I)_{x,\,\mathrm{eq}}}{(L^0)^3}}_{K_{\mathrm{eq}}}\,\delta_T, \tag{10}$$

where $(E\,I)_{x,\,\mathrm{eq}}$ is the equivalent flexural rigidity of the actuator in the x-axis direction, L^0 is the deformed length of the actuator at mid-plane, and δ_T is the tip deflection from Eq. (9). The equivalent flexural rigidity $(E\,I)_{x,\,\mathrm{eq}}$ is obtained by solving Eq. (A.9) [75, 95, 96]:

$$(E\,I)_{x,\,\mathrm{eq}} = \frac{\det\left(\begin{bmatrix} [\mathbf{A}] & [\mathbf{B}] \\ [\mathbf{B}] & [\mathbf{D}] \end{bmatrix}\right) w}{\det\left(\begin{bmatrix} [\mathbf{A}] & [\mathbf{B}] \\ [\mathbf{B}] & [\mathbf{D}] \end{bmatrix}_{4,4}\right)}, \tag{11}$$

where the matrices $[\mathbf{A}]$, $[\mathbf{B}]$, and $[\mathbf{D}]$ are the extensional stiffness matrix (A.10), the extension-bending coupling matrix (A.11), and the bending stiffness matrix (A.12), respectively (for details, see Appendix A). The $[\mathbf{AB},\mathbf{BD}]_{4,4}$ is obtained by removing the 4th row and the 4th column from the assembled $[\mathbf{AB},\mathbf{BD}]$ matrix, and w is the width of the actuator.

In the subsequent analytical model of the actuator, the equivalent bending stiffness in Eq. (10) will be denoted as K_{eq} for brevity.

2.3. Stress Relaxation of Polymers

Stress relaxation is the gradual decrease in stress when a material is held at constant strain [71, 72, 73, 97]. For a linear viscoelastic material, the ratio of the stress relaxation $\sigma(t)$ at a constant strain magnitude ε_0 to the strain is described by the relaxation modulus [71, 97]:

$$E(t) = \frac{\sigma(t)}{\varepsilon_0}. \tag{12}$$

The relaxation modulus $E(t)$ can be modeled using a Prony series with N terms as [97, 98, 99]:

$$E(t) = E_0 \left[1 - \sum_{k=1}^{N} r_k \left(1 - e^{-\frac{t}{\tau_k}} \right) \right], \tag{13}$$

where E_0 is the instantaneous value, *i.e.*, the elastic modulus, and the sum over N Prony terms includes the relative relaxation term r_k and the corresponding characteristic time τ_k, which are obtained by fitting the Prony series to experimental data.

The speed of the stress relaxation depends on the temperature, making the relaxation modulus a function of both temperature T and time t. Using time–temperature superposition, the relaxation modulus can be expressed as [100]:

$$E(t, T) = E(\zeta,\ T_{\mathrm{ref}}), \tag{14}$$

where ζ is the reduced time and T_{ref} is the reference temperature. The reduced time is defined as [97, 98]:

$$\zeta = \frac{t}{a_T(T)}, \tag{15}$$

where $a_T(T)$ is the shift-factor. The shift-factor $a_T(T)$ represents a horizontal time–temperature shift of the material property curves on the log-time axis for a given temperature change [97, 98, 99]. For polymer materials, the shift-factor $a_T(T)$ tends to follow the empirical Williams-Landel-Ferry (WLF) equation [97, 98, 99]:

$$\log_{10} a_T(T) = -\frac{C_1(T - T_{\mathrm{ref}})}{C_2 + (T - T_{\mathrm{ref}})}, \tag{16}$$

where T_{ref} is the reference temperature of the constructed curve by time–temperature shift, and the constants C_1 and C_2 depend on the specific polymer material.

For an arbitrary strain history $\{\boldsymbol{\varepsilon}(t)\}$ as a function of time t, the resulting time-dependent stresses $\{\boldsymbol{\sigma}(t)\}$ are obtained by solving the hereditary integral [98, 100, 101]:

$$\{\boldsymbol{\sigma}(t)\} = \int_0^t [\mathbf{R}(t-\tau)] \frac{\mathrm{d}\{\boldsymbol{\varepsilon}(\tau)\}}{\mathrm{d}\tau} \mathrm{d}\tau, \tag{17}$$

where $[\mathbf{R}(t-\tau)]$ is the time-dependent stiffness matrix. For orthotropic materials under the plane-stress assumption, $[\mathbf{R}(t-\tau)]$ is represented by a symmetric 3×3 matrix, with each component being an individual relaxation function approximated by a Prony series (Eq. (13)).

3. Single-Process 3D-Printed Bimorph Electrothermal Actuators

This section introduces the design and 3D-printing procedure for the single-process, 3D-printed, bimorph, electrothermal actuator. Subsequently, the proposed analytical model for tip deflection and blocking force is presented.

Fig. 3a shows the single-process, 3D-printed, bimorph, electrothermal actuator. The actuator consists of three material layers: the 1st material layer (M1) has a high CTE, the 2nd material layer (M2) serves as a heater made of electrically conductive material, and the 3rd material layer (M3) has a low CTE. Each layer has a thickness t_i, as shown in the schematic model in Fig. 3b. The actuator has an active length L, with an additional length L_c for clamping to ensure a fixed boundary condition, and a width w. The heater (M2) is divided in the middle by an electrically non-conductive material, *i.e.*, insulating material (IM), with a width $w_g = w - 2 \cdot w_h$ and a length $L_g = L + L_c - w_h$, creating an electrically conductive path with a width w_h. It is important that the size of w_g is sufficient to electrically insulate the two parts of the heater. This design provides a large contact area between M1, M3, and the heater to heat the actuator efficiently and evenly, while maintaining a low resistance.

3.1. 3D-Printing Electrothermal Bimorph Actuator

Fig. 3a shows the step-by-step, single-process, 3D-printing of the electrothermal actuator, with material deposition (indicated by the blue line) in each material layer. The material layers are stacked along the z-axis of the 3D printer, aligning the z-axis of both the actuator and the 3D-printer. First, M1 is 3D-printed with material deposited along the y-axis. This orientation achieves a higher thermal expansion in the x-axis by utilizing the higher CTE in the 2nd principal axis, as indicated by previous research [69]. Additionally, printing M1 first helps prevent warping of the actuator on the print bed during cooling. Next, M2 and insulating material are printed with the material deposited along the x-axis to leverage the lower electrical resistivity of the conductive material in the 1st principal axis direction [102]. 3D-printing insulating material in the x-axis direction prevents short circuits by pulling the previously deposited M2 material across the insulating

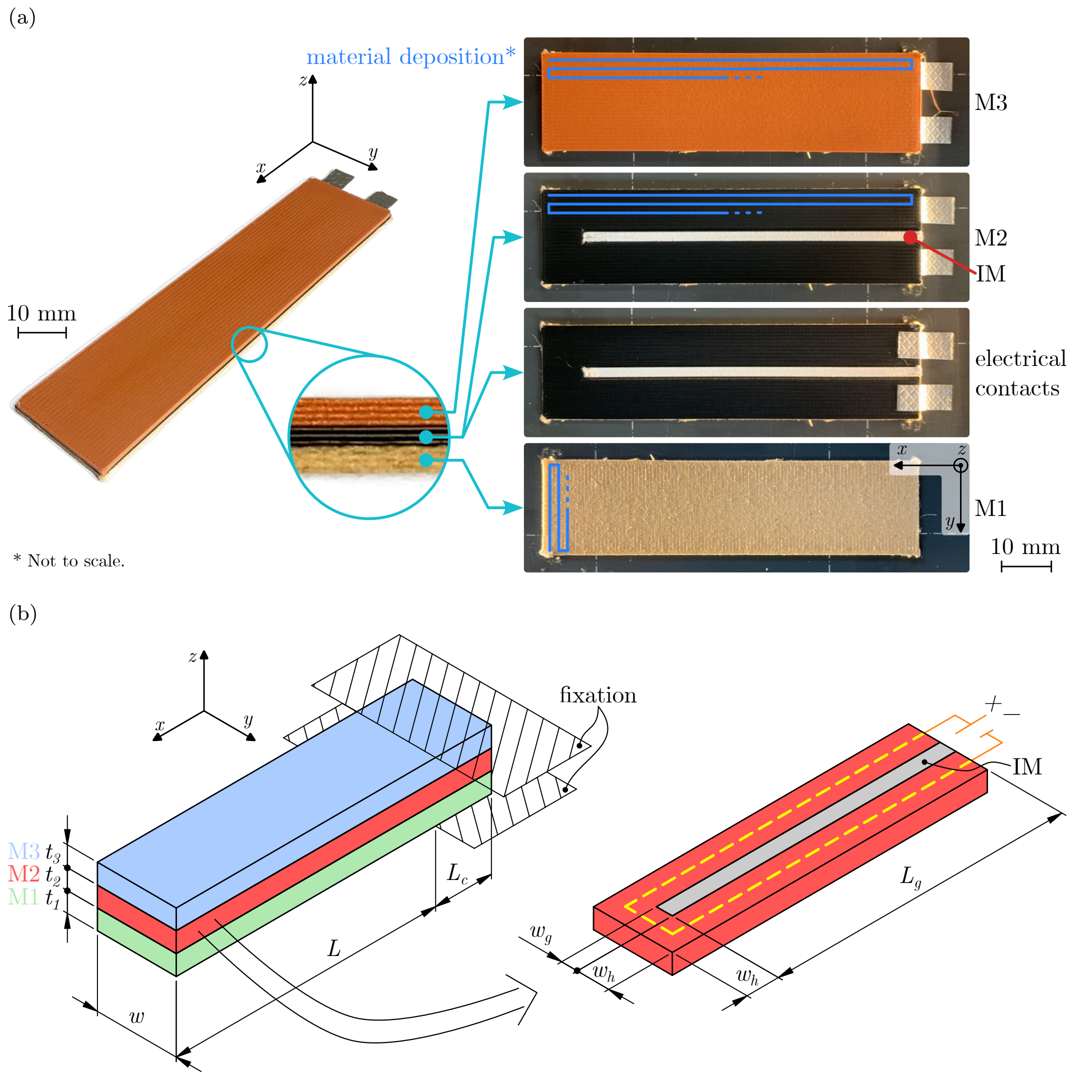

Figure 3: (a) Step-by-step single-process 3D printing of a bimorph electrothermal actuator, illustrating the layer-by-layer deposition of M1 (high CTE), M2 (heater) with insulating material (IM), and M3 (low CTE). Each layer is oriented to optimize thermal or electrical properties, and electrically conductive tape is embedded to provide robust electrical contacts. (b) Schematic of the final actuator geometry, showing the heater's conductive path separated by an insulating gap. The stacked layers are aligned along the 3D printer's z-axis, enabling single-process fabrication without additional assembly.

gap. After 3D-printing the first layer of M2, electrically conductive tape is bonded to it. Conductive material is then deposited over the tape in the subsequent 3D-printed layer of M2 to ensure good electrical contact, as shown in Fig. 3a. Finally, M3 is 3D-printed with the material deposited along the x-axis to achieve lower thermal expansion by utilizing the lower CTE in the 1st principal axis direction [69].

It is important to use compatible materials to achieve strong bonds at common surfaces, ensuring they can withstand shear forces during actuation. Additionally, to support the assumptions in the subsequent analytical model, M2 and the insulating material should have similar mechanical and thermal properties–specifically, similar elastic moduli, CTEs, and thermal conductivities. This allows the model to treat the M2/insulating material layer as effectively homogeneous, thereby simplifying the analytical model by ensuring a uniform temperature distribution and consistent strain across the material layer.

3.2. Analytical model

The analytical model for the time-dependent tip deflection and blocking force of a single-process 3D-printed multilayer electrothermal actuator is developed in three steps:

1. **Transient thermal analysis**: The time-dependent temperature distribution within the 3D-printed electrothermal actuator is calculated under the applied voltage.
2. **Tip deflection computation**: The tip deflection as a function of time is evaluated for each temperature distribution at each time-step, using updated temperature-dependent mechanical properties.

3. **Blocking force computation**: The generated blocking force as a function of time is determined for each temperature distribution at each time-step, accounting for stress relaxation.

The proposed model employs a decoupled thermomechanical approach, in which a transient thermal analysis first computes the time-dependent temperature distribution. This temperature profile is then used to update temperature-dependent mechanical properties, such as elastic moduli and stiffness matrices, for the subsequent mechanical analysis. The sequential formulation simplifies the modeling process while capturing the essential thermomechanical behavior of the actuator. Fig. 4 is a representation of the analytical model, showing the input and output parameters.

Thermal Model. To obtain the time-dependent temperature distribution in the 3D-printed, electrothermal actuator in the z-axis direction, a simplified one-dimensional model with three material layers, internal heat generation in the second material layer, and convection boundary conditions is built, as shown in Fig. 5. The thermal model assumes a uniform temperature in the x-y plane (see Fig. 3b), achieved by the large contact heater, and that the 2nd material layer consists only of M2, neglecting the effect of the insulating material.

Due to the complexity of the problem, a numerical solution of the heat equation (1), such as the finite-differences method [82, 103], is required for each material layer. The thermal conductivity k in the z-axis direction is needed (see Fig. 5) for each material layer, which, based on the orientation of the 3D-printed electrothermal actuator (see Fig. 3a), corresponds to the material properties in the direction of the 3rd principal axis. Additionally, the

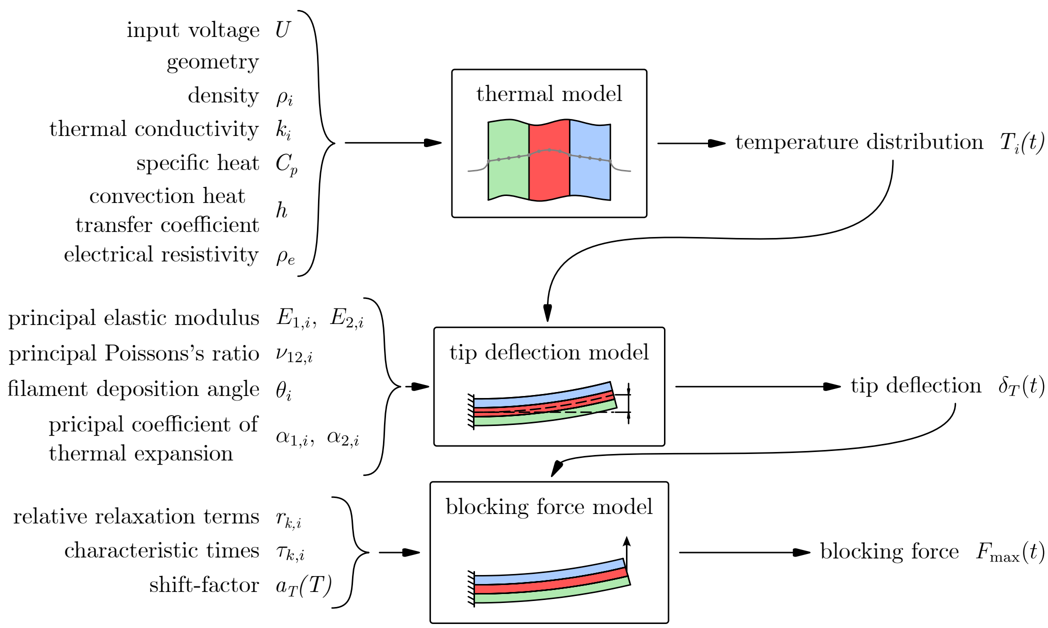

Figure 4: Block diagram of the decoupled thermomechanical approach for predicting the time-dependent tip deflection and blocking force of a single-process 3D-printed bimorph electrothermal actuator. A transient thermal model computes the temperature distribution from the input voltage, followed by the update of temperature-dependent mechanical properties to compute tip deflection. Stress relaxation is then incorporated to determine the time-varying blocking force. This sequential approach captures the actuator's thermomechanical response.

mass density ρ and specific heat C_p of the material layers are required for the thermal model. The continuity of the temperature (7) and the heat flux (8) is preserved at the common surfaces between M1 and M2, as well as M2 and M3. On the outer surfaces of M1 and M3, only the convection boundary condition (6) is applied, as radiation is negligible within the temperature range considered in this study [68, 82, 30]. The convection heat-transfer coefficient h for passive convection at room temperature ($T_\infty = 22\,^\circ\mathrm{C}$) is

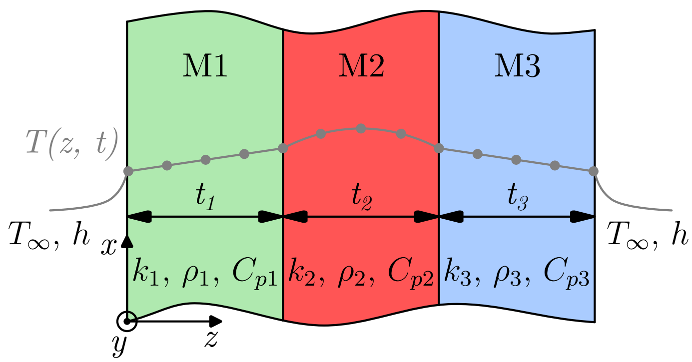

Figure 5: One-dimensional thermal model of the three-layer actuator, assuming uniform properties in the x–y plane and internal heat generation in the middle layer. Each layer is assigned thermal properties along the z-axis, with convective boundary conditions applied at the outer surfaces.

used.

The Joule heating of the actuator at an applied voltage U is modeled by the internal heat generation within the second material layer, as described by Eq. (3). The electrical resistance of the heater R is estimated using Eq. (4). For the length of the resistor l, the average length of the electrically conductive path is chosen, as indicated by the yellow dashed line in Fig. 3b. The heater has a rectangular cross-section with an area of $A = w_h \cdot t_2$ (see Fig. 3b). For simplicity, it is assumed that the electrical resistivity ρ_e is uniform along the entire conductive path and does not change with temperature within the considered range. Due to the dimensions of the actuator ($L > w$), the conductive path is primarily in the x-axis direction, corresponding to the 1st principal axis (see the material deposition of M2 in Fig. 3a). Hence, the electrical resistivity ρ_e in the 1st principal axis direction is used. Therefore, the theoretical electrical resistance of the actuator heater is determined using

Eq. (4) as follows:

$$R_{h,\mathrm{theo}} = \rho_e \frac{2\,(L+L_c)+w-2\,w_h}{w_h\,t_2}. \tag{18}$$

When the actuator is 3D-printed, the actual resistance R_h of the heater is measured and used in the model. For simplicity, it is assumed that the electrical resistance remains constant over the operating temperature range. However, if the temperature dependence of resistance is known, it can be updated and accounted for at each time-step. The energy-generation rate per unit volume $\dot{q}$ of the heater at an applied voltage U, used in the heat equation (1) for the 2nd material layer, is determined from Eq. (2) using the volume of the entire 2nd material layer:

$$\dot{q} = \frac{U^2}{R_h[(L+L_c)\,w\,t_2]}. \tag{19}$$

Tip Deflection. To obtain the time-dependent tip deflection of the 3D-printed electrothermal actuator with fixed-free boundary conditions, a three-layer laminate model is built, as shown in Fig. 2. Similar to the thermal model, the insulating material is neglected, and it is assumed that the 2nd material layer consists only of M2. The tip deflection is determined using Eq. (9) by utilizing the CLT with the plane stress assumption (for details, see Appendix A). The curvature in the x-axis direction κ_x and the mid-plane strain ε_x of the laminate are determined for thermal loads based on the temperatures at each time-step from the thermal model, and L represents the active length of the actuator (see Fig. 3b).

To obtain the curvatures κ_x and mid-plane strains ε_x, the in-plane stiffness matrix for each material layer is first constructed using Eq. (A.3). The elastic modulus in the 1st and 2nd principal axes (E_1 and E_2), Poisson's ratio in the 2nd principal axis when a load is applied in the 1st direction ν_{12}, and the angle of material deposition θ for each material layer are used. Based on the filament deposition of material layers discussed in Sec. 3.1, the angles are $\theta_1 = \pi/2$ and $\theta_2 = \theta_3 = 0$ for M1, M2, and M3, respectively. For actuators with material deposition angles $\theta_k = 0$ or $\theta_k = \pm\pi/2$ and no applied shear stresses, the shear modulus G_{12} is not required. The temperature dependence of the mechanical properties is accounted for by updating them at each time-step based on the temperature determined by the thermal model and recalculating the stiffness matrices. Second, the in-plane stiffness matrices are combined into the laminate's extensional stiffness matrix $[\mathbf{A}]$ Eq. (A.10), extension-bending coupling matrix $[\mathbf{B}]$ Eq. (A.11), and bending-stiffness matrix $[\mathbf{D}]$ Eq. (A.12), where

$$\bar{z}_1 = -\frac{t_2}{2} - \frac{t_3}{2},\ \bar{z}_2 = \frac{t_1}{2} - \frac{t_3}{2},\ \bar{z}_3 = \frac{t_1}{2} + \frac{t_2}{2}. \tag{20}$$

Third, the thermal forces and moments in the laminate are determined for the temperature at each time-step from the thermal model. The temperature difference of the average spatial temperature in each layer $\Delta\overline{T}_k$ is calculated from the thermal model and used in Eq. (A.13) and (A.14). Finally, Eq. (A.15), with no external loads, is solved at each time-step to obtain the mid-plane strains $\{\boldsymbol{\varepsilon}^{\mathbf{0}}\}$ and curvatures $\{\boldsymbol{\kappa}\}$ of the laminate over time. The time-dependent tip deflection is then determined using Eq. (9).

Blocking Force. To obtain the time-dependent blocking force of the 3D-printed, electrothermal actuator with fixed-free boundary conditions, the same three-layer laminate model used for tip deflection is employed (Fig. 2). However, the output force of the actuator is influenced by the stress relaxation of the polymer materials, as discussed in Sec. 2.3. Therefore, to determine the time-dependent blocking force, the hereditary integral (Eq. (17)) is applied in Eq. (10) as follows:

$$F_{\max} = \int_0^t K_{\mathrm{eq}}(t-\tau)\frac{\mathrm{d}\delta_T(\tau)}{\mathrm{d}\tau}\mathrm{d}\tau, \tag{21}$$

where K_{eq} is the equivalent bending stiffness of the actuator, which is time- and temperature-dependent, and δ_T is the previously determined tip deflection. The time dependence of the equivalent bending stiffness is accounted for by using the principal relaxation moduli $E_i(t)$, approximated by the Prony series (Eq. (13)), when constructing the stiffness matrices in Eq. (11), in the same manner as for the tip deflection. The temperature dependence of the equivalent bending stiffness is incorporated by using a reduced time for the principal relaxation moduli (Eq. (14)). The deformed length of the actuator at the mid-plane, $L^0 = L(1+\varepsilon_x^0)$, is determined from the initial length of the actuator L and the mid-plane strains in the x-axis direction ε_x^0, based on the tip-deflection results.

Since the temperatures, tip deflection δ_T, and mid-plane strain ε_x^0 are determined at N discrete points with a time interval Δt, Eq. (21) is expressed in discrete form as follows:

$$F_{\max}[n] = K_{\mathrm{eq}}[0]\,\delta_T[0] + \sum_{m=1}^{n} K_{\mathrm{eq}}[n-m]\Delta\delta_T[m]\,;\ n = 1,\ 2\ ...\ N, \tag{22}$$

where $F_{\max}[n]$ is the blocking force at the discrete time-step $t[n]$, $K_{\mathrm{eq}}[0]$ and $\delta_T[0]$ are the initial (time-step $t[0]$) equivalent bending stiffness and tip deflection, respectively, $K_{\mathrm{eq}}[n-m]$ is the equivalent bending stiffness at the discrete time-step $t[n-m]$, and $\Delta\delta_T[m] = \delta_T[m] - \delta_T[m-1]$ is the change in tip deflection at the time-step $t[m]$. The equivalent bending stiffness at the discrete time-step $t[n-m]$ is determined according to Eq. (10) as:

$$K_{\mathrm{eq}}[n-m] = \frac{3\,(E\,I)_{x,\,\mathrm{eq}}[n-m]}{\{L(1+\varepsilon_x^0[n])\}^3}, \tag{23}$$

where $(E\,I)_{x,\,\mathrm{eq}}[n-m]$ is the equivalent flexural rigidity at time-step $t[n-m]$, and $\varepsilon_x^0[n]$ is the mid-plane strain in the x-axis direction at time-step $t[n]$. The equivalent flexural rigidity $(E\,I)_{x,\,\mathrm{eq}}[n-m]$ is determined using Eq. (11) with time- and temperature-dependent principal relaxation moduli at time-step $t[n-m]$ as (Eq. 14):

$$E_i(t[n-m],\ T[n]) = E_i(\zeta[n-m],\ T_{\mathrm{ref}}). \tag{24}$$

Here, the reduced time-step $\zeta[n-m]$ is based on the time increment $t[n]-t[m]$ and the shift-factor at the temperature at time-step $t[n]$, as follows (Eq. (15)):

$$\zeta[n-m] = \frac{t[n]-t[m]}{a_T(T[n])}. \tag{25}$$

The WLF equation (16) is used to determine the shift-factor $a_T(T[n])$.

In this way, the convolution in Eq. (22) is used to obtain the force at each time-step, and thereby the time-dependent blocking force of the actuator.

4. Experimental Research

This section presents details of the 3D-printing of the introduced, single-process, 3D-printed, bimorph, electrothermal actuator. Subsequently, the experimental setup for validation of the proposed analytical model for tip deflection and blocking force is presented.

The actuators and all the samples to determine the material properties were printed on an E3D Toolchanger 3D-printer to utilize multi-material,

Table 1: Used materials with their print settings.

Filament	Manufacturer	Refered to as	Print Settings Nozzle Temp. [°C]	Bed Temp. [°C]	Print Speed [mm/s]
Nylon PA12+CF15	Fiberlab	PACF	260	90	60
Nylon PA12+GF15	Fiberlab	PAGF	255	90	60
Prusament PLA	Prusa Polymers	PLA	215	60	60
Conductive PLA	Protopasta	condPLA	215	60	40
EasyWood Cedar	Formfutura	woodPLA	215	60	60
StoneFil Terracotta	Formfutura	stonePLA	220	60	60
Eel 3D Printing Filament	NinjaTek	condTPU	225	45	20
Ice9 Insulating	TCPoly	thermalTPU	230	45	30

thermoplastic extrusion, 3D-printing for manufacturing in a single-process. They were printed with a 0.4-mm nozzle, 0.42-mm extrusion width, 0.2-mm layer height, 100 % fill density, aligned rectilinear fill pattern and a single perimeter. Further filament-specific settings can be found in Tab. 1.

4.1. 3D-Printing Electrothermal Bimorph Actuator

The proposed approach (see Sec. 3) was used to manufacture electrothermal bimorph actuators in two distinct configurations, denoted as A1 and A2. Material and geometrical details are provided in Tab. 2. While the overall dimensions–length, width, and thickness–remain similar, individual layer thicknesses were adjusted to optimize performance for each material combination. The two configurations, A1 and A2, were selected to evaluate the impact of different material combinations on actuator performance and to validate the robustness of the proposed analytical model. Configuration A1 was designed to maximize thermal expansion mismatch by selecting ma-

Table 2: 3D-printed electrothermal bimorph actuators.

Actuator	Material Layer	Material	t_i [mm]	L [mm]	w [mm]	w_h [mm]	L_c [mm]
A1	M1	PAGF	0.6	60	20	9	20
	M2	condTPU	1.2				
	M3	PACF	0.6				
	IM	thermalTPU	1.2				
A2	M1	woodPLA	0.8	60	20	9	20
	M2	condPLA	0.6				
	M3	stonePLA	0.8				
	IM	PLA	0.6				

terials with the greatest difference in CTE between M1 and M3, resulting in pronounced tip deflection. In this setup, the heater is made from conductive TPU, which offers high conductivity, effective bonding with PA-based materials, and, due to its soft core, enables large actuator deformation. In contrast, configuration A2 uses PLA-based materials for all material layers to ensure strong interlayer bonding. This configuration exhibits lower thermal expansion and stiffness, as well as higher temperature dependence, thereby providing a contrasting behavior to test the model's predictive capabilities across different material systems.

Fig. 3a shows the layer-by-layer process of 3D-printing the A2 actuator. M1 was printed with a fill angle of 90°, while M2, M3, and insulating material were printed with a fill angle of 0° to achieve the desired material-deposition orientation, leveraging orthotropic material properties to maximize the thermal expansion differences and minimize the heater resistance. An electrically conductive tape with 5-mm overlap was used for the electrical contacts.

The 3D-printing process took approximately 30 min per actuator. For each configuration (A1 and A2), three independent specimens were manufactured to account for any variability inherent in the 3D-printing process.

4.2. Mechanical Characterization of 3D-printed Electrothermal Bimorph Actuator

Fig. 6 shows the experimental setup for measuring the tip deflection and blocking force. After 3D-printing, the actuator was clamped the length L_c (see Fig. 3b). The clamping fixture, secured with two screws, ensured a fixed boundary condition and held the actuator in a horizontal position. A DPPS-60-10 (Voltcraft, Germany) power source was connected to the actuator's electrical contacts using crocodile clips. The surface temperature was measured using a FLIR A50 (Flir, USA) thermal camera.

For the tip-deflection measurements, the VibroGo VGO-200 (Polytec, Germany) laser vibrometer was used to measure the displacement, as shown in Fig. 6a. During the tip-deflection measurement, the force sensor was removed to allow the actuator to bend freely.

To measure the blocking force, an FX293X-100A-0025-L (TE Connectivity, Switzerland) load cell was employed to measure the force at the actuator's tip, as shown in Fig. 6b. The load cell was attached to a customized positional bracket, allowing accurate placement at the center of the actuator's width. A metal pin was added to the load cell to ensure point contact with the actuator. Before the blocking-force measurement, the actuator's tip was positioned on the load cell to ensure initial contact.

Both the laser-vibrometer and load-cell signals were recorded using the NI-9215 (National Instruments, USA) measurement card. Prior to each mea-

(a)

(b)

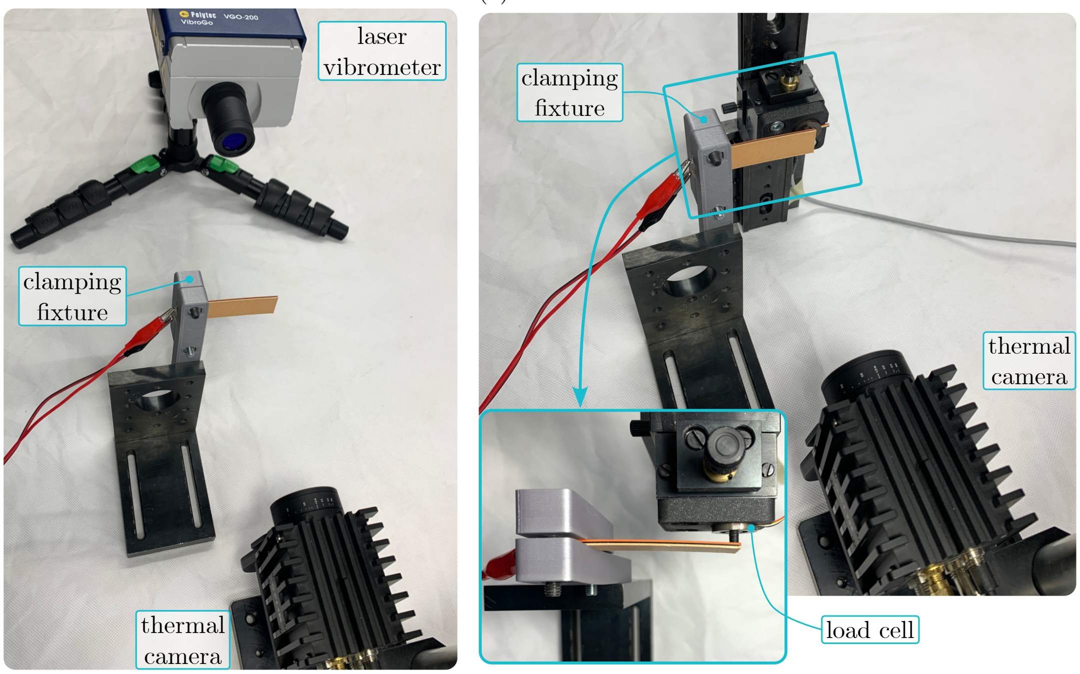

Figure 6: (a) Experimental setup for measuring the tip deflection of the 3D-printed actuator using a laser vibrometer. The actuator is clamped at one end to provide a fixed boundary, and a thermal camera monitors the surface temperature. (b) Setup for blocking force measurement, with a load cell positioned at the actuator tip. In both experiments, a step voltage is applied to the actuator.

surement, the actuator was cooled until it stabilized to room temperature (22 °C) to ensure consistent initial conditions. A step voltage of $U = 48\,\mathrm{V}$ was applied to the actuator, triggering thermal image acquisition and displacement or force measurement. Signals were recorded for 10 min, allowing the actuator temperature to reach a steady state. The average temperature was defined from an area 1 mm away from all the edges of the actuator to exclude boundary effects.

The analytical model of the 3D-printed, bimorph, electrothermal actuator, proposed in Sec. 3.2, was used to predict the tip deflection and blocking force of the A1 and A2 actuators (see Tab. 2) for experimental validation.

Initially, the required input material parameters were determined (see Fig. 4). The material properties of 3D-printed structures depend on various manufacturing and structural parameters, as well as time and temperature, as described in Sec. 2. Therefore, the material properties are best determined experimentally. An efficient experimental identification of the required material properties along their respective principal axes was conducted to obtain the necessary input parameters for the analytical model. To keep the main text concise and focused, the details of the experimental setup and the methodology for material property identification are provided in Appendix B. The determined material properties are presented in Tab. 3. These material properties, along with the actuator geometry (see Tab. 2), served as inputs for the model.

First, the temperature distribution was calculated for an applied voltage of $U = 48\,\mathrm{V}$. A thermal model, based on the implicit finite-difference method [82, 103], was used with 6 nodes per material layer and a time-step of 1 s. The measured electrical resistance of the heater R_h, a convection coefficient of $h = 12\,\mathrm{W\,m^{-2}\,K^{-1}}$ [104], and an ambient temperature of 22 °C were included. The initial temperature was set to 22 °C, and the resulting temperature distribution was computed over the experimental timeframe, and the surface node temperature was compared to the experimentally measured average surface temperature.

Next, the calculated temperature distribution was used to predict the tip deflection δ_T. For each time-step, the average spatial temperature in each

Table 3: Identified material properties needed for thermal, tip deflection and blocking force model.

Material Property	Unit	A1			A2		
		PAGF	condTPU	PACF	woodPLA	condPLA	stonePLA
ρ	kg/m^3	1000	1180	931	1013	1240	1432
k	$W\,m^{-1}\,K^{-1}$	0.11	0.14	0.11	0.15	0.17	0.24
C_p	$J\,kg^{-1}\,K^{-1}$	1474	1212	1119	1124	1019	1034
ρ_e	$\Omega\,cm$	/	34	/	/	19	/
E_1	GPa	3.22	0.08	5.38	2.01	2.43	5.8
E_2	GPa	1.52	0.07	1.61	1.27	1.92	2.07
ν_{12}	/	0.44	0.5	0.48	0.32	0.4	0.38
α_1	$\mu m\,m^{-1}\,K^{-1}$	45.4	174	18.7	89.1	109	24.1
α_2	$\mu m\,m^{-1}\,K^{-1}$	138	388	134	98.1	204	204
r_1	/	0.18	0.15	0.16	0.05	0.75	0.02
r_2	/	0.6	0.2	0.44	0.64	0.25	0.57
r_3	/	/	0.6	/	0.16	/	0.24
τ_1	s	1004	1030	956	810	31854	280
τ_2	s	16334	12090	16504	24150	132054	12050
τ_3	s	/	131521	/	84784	/	81741
C_1	/	3.7	3.9	4.6	7.9	7.1	26
C_2	°C	22	34	39	61	41	196
T_{ref}	°C	22	22	22	22	22	22

material layer $\overline{T}$ was calculated as the average temperature in the six nodes, and further the temperature difference $\Delta\overline{T}$ relative to the initial temperature. Based on $\overline{T}$, the elastic moduli E_i were updated to account for the temperature dependence, while Poisson's ratios ν_{12} were assumed to remain constant. The stiffness matrices ([**A**], [**B**], [**D**]) and thermal loads were calculated for each time step, from which the curvatures κ_x and mid-plane deformations ε_x^0 were obtained. Using κ_x and ε_x^0, the time-dependent tip deflection δ_T was estimated, and compared to the experimental results.

Finally, the blocking force $F_{\max}$ was estimated. For each time-step $t[n]$, the convolution of the stress relaxation was calculated using the WLF equation to determine the reduced time-step $\zeta[n-m]$ based on the average spatial temperature $\overline{T}[n]$. The relaxation moduli $E_i(t[n-m])$ were computed and used to update the stiffness matrices, which yielded the equivalent flexural rigidity $(E\,I)_{x,\mathrm{eq}}[n-m]$ and bending stiffness $K_{\mathrm{eq}}[n-m]$. The same relaxation model was applied to both principal axes, as the orientation has minimal influence on the stress relaxation behavior [72]. The Poisson's ratios were assumed to be constant with respect to time and temperature. The equivalent flexural rigidity $K_{\mathrm{eq}}[n-m]$ was multiplied by the change in tip deflection during the previous time-step, $\Delta\delta_T[m]$, to compute the partial blocking forces. Partial blocking forces from previous time-steps, adjusted for stress relaxation, were summed to compute the time-dependent blocking force $F_{\max}$, which was compared to the experimental measurements.

5. Results and Discussion

This section presents the measured temperature, tip deflection, and blocking force of the proposed single-process 3D-printed bimorph electrothermal actuator and compares the results with predictions from the analytical model. In addition, a comprehensive sensitivity analysis is conducted to evaluate the influence of key input parameters on both thermal and mechanical responses.

A total of six electrothermal actuators were experimentally characterized: three with the A1 configuration and three with the A2 configuration (see Tab. 2), to validate the reliability of the single-process, 3D-printing method for bimorph, electrothermal actuators.

Fig. 7a shows the measured average temperature on the outer surface of M1 for both A1 and A2 actuators, along with the temperature predicted by the proposed analytical model. All actuators exhibit similar thermal behavior, and the proposed thermal model (see Sec. 3) accurately predicts the surface temperature. It is assumed that the proposed thermal model also accurately predicts the internal temperature distribution within the actuator.

The measured tip deflection of the cantilever bimorph electrothermal actuators is shown in Fig. 7b. Actuators of the same configuration exhibit similar tip deflection. Additionally, the tip deflection predicted by the conventional model described in [77] (gray solid line) and by the proposed analytical model (red solid line) are shown. Both the conventional and proposed models produce similar tip-deflection predictions, which align well with the experimental data.

Fig. 7c presents the measured blocking force of the cantilever bimorph electrothermal actuators. Again, actuators of the same configuration exhibit similar blocking-force behavior. Additionally, the blocking force predicted by the conventional model [77] (gray solid line) and the proposed analytical model (red solid line) are included. For both configurations, the conventional model inaccurately predicts a higher blocking force that converges to a constant value with time. However, due to the stress relaxation in polymers, which is accelerated at elevated temperatures, the blocking force decreases over time when a constant voltage is applied to the actuator. The proposed model accounts for stress relaxation, accurately capturing the drop in blocking force caused by the temperature- and time-dependent changes in stiffness.

(a)

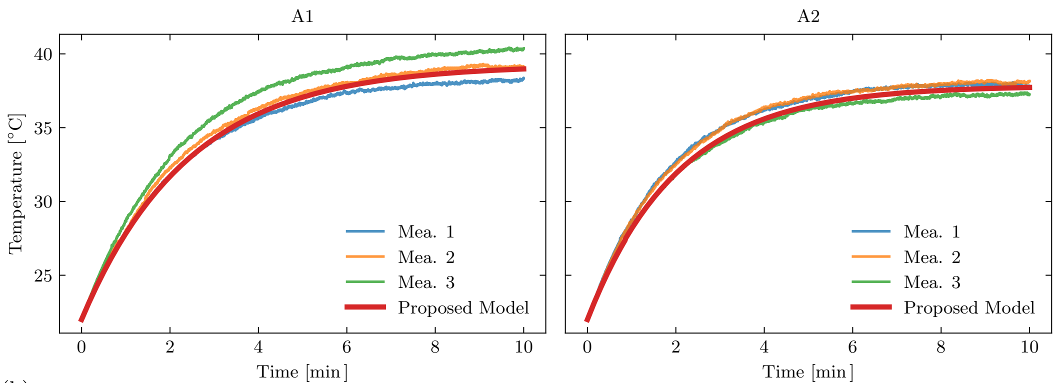

(b)

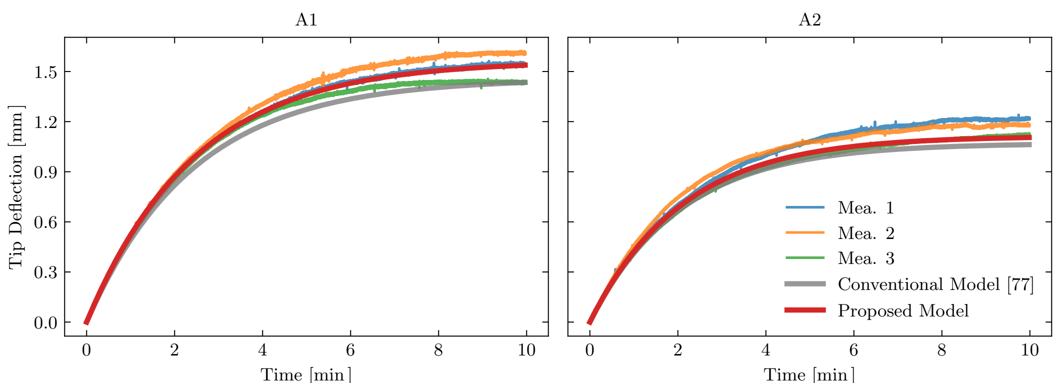

(c)

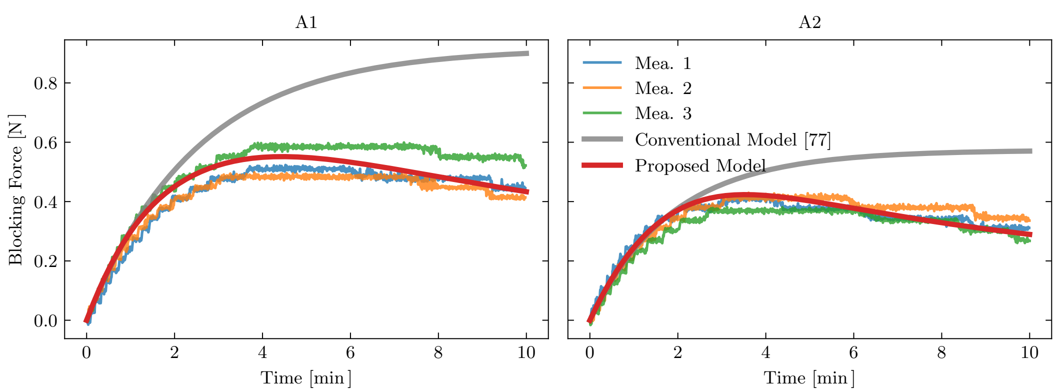

Figure 7: Measured and predicted responses of A1 (left) and A2 (right) electrothermal actuators: (a) average temperature on the outer surface of M1, comparing measurements (Mea.) with the proposed analytical model; (b) tip deflection, comparing measurements (Mea.), the conventional model [77] (gray), and the proposed model (red); and (c) blocking force, also compared among measurements (Mea.), the conventional model (gray), and the proposed model (red).

This allows for accurate modeling of single-process thermoplastic extrusion 3D-printed electrothermal actuators, which is essential for applications in smart structures.

The proposed actuator design has a characteristic actuation time of $\tau = 148\,\mathrm{s}$ and $\tau = 126\,\mathrm{s}$ for the A1 and A2 actuators, respectively. Due to the long activation time resulting from the low thermal diffusivity, this design is unsuitable for fast real-time applications such as artificial muscles or soft grippers. However, the proposed actuators and model serve as the foundation for future development and optimization of single-process electrothermal actuators. Faster actuation times can be achieved by implementing geometric features, such as ribs, to enhance heat transfer.

While the proposed analytical model and experimental validation demonstrate the potential of single-process 3D-printed electrothermal actuators, few simplifying assumptions were introduced to enable efficient and tractable modeling. These include a uniform temperature distribution in the x–y plane, similar mechanical and thermal properties for the heater (M2) and insulating material, constant heater resistance, and ideal layer bonding. The current model also focuses on rectangular geometries and linear elastic behavior. These assumptions are appropriate for the actuator design and are supported by experimental results; however, they define the current scope of the model. Importantly, they also suggest clear opportunities for future refinement, such as capturing localized temperature gradients, incorporating temperature-dependent resistance, modeling more complex geometries, and accounting for inter-layer deformability. Overall, these simplifications support a robust and validated framework while identifying promising directions to further enhance model accuracy and broaden applicability.

Nonetheless, the proposed design of single-process 3D-printed electrothermal actuators still holds significant potential for smart shape-morphing structures that actively modulate their shape in response to external loads in slowly changing environments. They can be integrated into metamaterials to actively tune properties such as stiffness, Poisson's ratio, and thermal expansion. Furthermore, given the design flexibility of thermoplastic extrusion 3D printing, this approach holds promise for developing lightweight, shape-adaptable, actively controlled smart structures manufactured in a single process.

Sensitivity Analysis. Fig. 8 presents the sensitivity of the actuator's thermal and mechanical responses–including steady-state surface temperature, transient temperature, tip deflection, and blocking force–to variations in key input parameters. Each parameter was varied independently while all others were held constant.

Fig. 8a illustrates that the steady-state surface temperature is most sensitive to the input voltage U, followed by layer thickness t, convective heat transfer coefficient h, electrical resistivity ρ_e, and ambient temperature T_∞. Due to the actuator's small thickness and large surface area, convective heat transfer dominates over conduction. Joule heating further amplifies sensitivity to U, t, and ρ_e. In contrast, density ρ, thermal conductivity k, and specific heat capacity C_p have little effect on steady-state temperature but do influence transient behavior at 60 s, as shown in Fig. 8b.

Fig. 8c shows that tip deflection is primarily governed by actuator geometry–specifically length L and thickness t. An increase in L results in greater deflection, while a larger t increases stiffness and reduces deformation. Temperature T and the CTE α also strongly affect deflection, with greater thermal expansion yielding larger tip displacement. In contrast, the elastic modulus E and Poisson's ratio ν have minimal influence.

Fig. 8d indicates that the maximum blocking force is most sensitive to actuator geometry–specifically thickness t, width w, and length L. Increasing t and w enhances stiffness, resulting in a higher blocking force, whereas increasing L reduces it. The CTE α and elastic modulus E also contribute to an increased blocking force by promoting internal stress generation. Temperature T has a moderate effect, while Poisson's ratio ν and stress relaxation parameters (r, τ, C_1, C_2) have little effect on the peak value but remain relevant for long-term force prediction.

Overall, actuator geometry–particularly thickness and length–and the CTE of the constituent materials significantly influence actuator performance. Accordingly, the proposed analytical model serves as a valuable tool for optimizing both geometry and material selection to achieve targeted performance in application-specific designs.

6. Conclusions

This research introduces the design principles and the analytical model for predicting the time-dependent tip deflection and blocking force of multilayered electrothermal actuators, 3D-printed in a single process. The fully 3D-printed actuator consists of three material layers: a high-CTE layer, a heater layer, and a low-CTE layer. The proposed analytical model incorporates orthotropic, temperature-dependent material properties and accounts

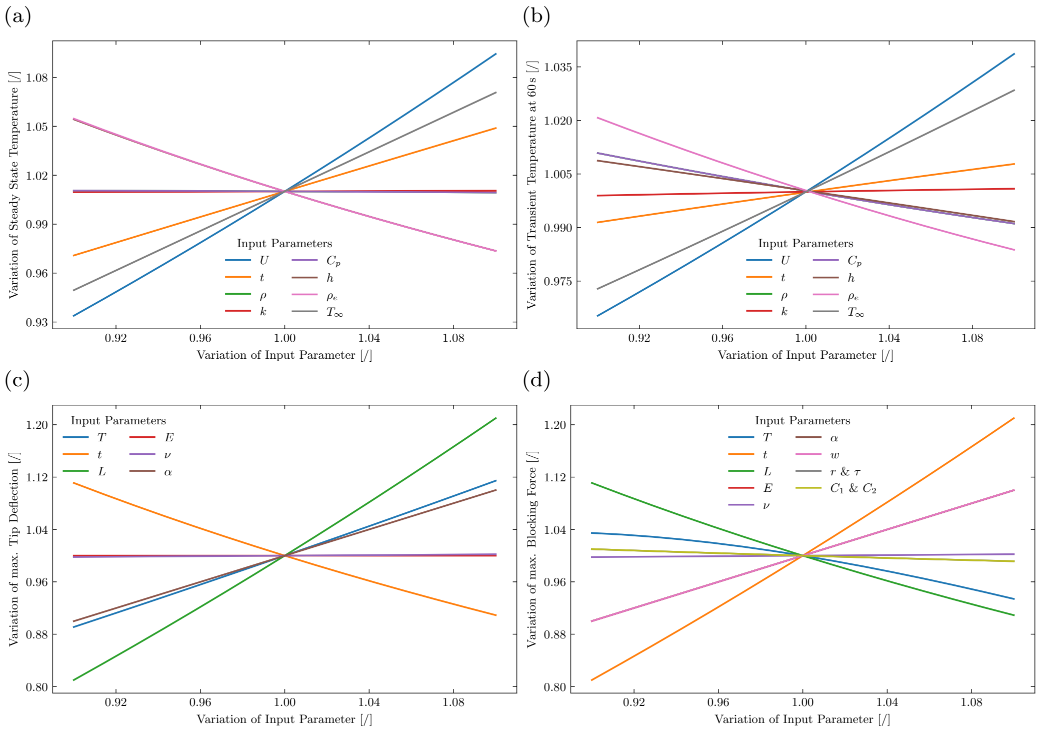

Figure 8: Parametric sensitivity analysis of the actuator's thermal and mechanical behavior in response to a $\pm 10\,\%$ variation in each input parameter, while all others are held constant. Subplots compare the relative influence of these parameters on: (a) steady-state surface temperature (note that ρ and C_p overlap, as do h and ρ_e); (b) transient temperature at $t = 60\,\mathrm{s}$ (with overlapping curves for ρ and C_p); (c) maximum tip deflection; and (d) maximum blocking force (with overlapping curves for E and w, as well as for α, r & τ, and C_1 & C_2).

for stress-relaxation effects. The proposed model predicts the time-dependent tip deflection and blocking force, given an input voltage. The model is experimentally validated using actuators manufactured with two distinct material configurations.

The actuator manufactured with PAGF, conductive TPU, and PACF material layers and dimensions of $60 \times 20 \times 2.4\,\mathrm{mm}$, achieved a temperature increase of $\Delta T = 17.0\,^{\circ}\mathrm{C}$ within $10\,\mathrm{min}$ under a step voltage of $48\,\mathrm{V}$. This resulted in a tip deflection of $1.5\,\mathrm{mm}$ with a characteristic actuation time $\tau = 148\,\mathrm{s}$ and a maximum blocking force of $0.55\,\mathrm{N}$ at $4.5\,\mathrm{min}$. The actuator manufactured with woodPLA, conductive PLA, and stonePLA material layers and dimensions of $60 \times 20 \times 2.2\,\mathrm{mm}$, achieved a temperature increase of $\Delta T = 15.7\,^{\circ}\mathrm{C}$ within $10\,\mathrm{min}$ under a step voltage of $48\,\mathrm{V}$. This resulted in a tip deflection of $1.1\,\mathrm{mm}$ with a characteristic actuation time $\tau = 126\,\mathrm{s}$ and a maximum blocking force of $0.42\,\mathrm{N}$ at $3.5\,\mathrm{min}$.

Experimental results confirm the repeatability and reliability of the single-process 3D-printing method. These actuators represent the first entirely single-process, 3D-printed, electrothermal actuators, which can be seamlessly integrated into smart structures, flexible electronics, and soft robotic systems. Furthermore, the proposed model accurately predicts the blocking force of thermoplastic extrussion 3D-printed electrothermal actuator by capturing the temperature- and time-dependent decrease in blocking force caused by the stress relaxation. Conventional model neglects these effects and at $10\,\mathrm{min}$ overestimate the blocking force by $108\,\%$ and $97\,\%$ for the two actuator experimentally researched.

The proposed design of single-process 3D-printed electrothermal actuators holds significant potential for smart shape-morphing structures that actively modulate their shape in response to external loads in slowly changing environments. The proposed model serves as the foundation for further research and development of single-process 3D-printed electrothermal actuators with faster actuation times, enabling further integration into active structures.

Acknowledgements

The authors acknowledge the partial financial support from the Slovenian Research Agency (research core funding No. P2-0263 and research project L2-60140).

The activities are implemented within the framework of the GREENTECH project, co-financed by the European Union – NextGenerationEU.

References

[1] I. Apsite, S. Salehi, L. Ionov, Materials for Smart Soft Actuator Systems, Chemical Reviews 122 (2022) 1349–1415. doi:10.1021/acs.chemrev.1c00453.

[2] M. Li, A. Pal, A. Aghakhani, A. Pena-Francesch, M. Sitti, Soft actuators for real-world applications, Nature Reviews Materials 7 (2022) 235–249. doi:10.1038/s41578-021-00389-7.

[3] Y. Shao, F. Long, Z. Zhao, M. Fang, H. Jing, J. Guo, X. Shi, A. Sun, G. Xu, Y. Cheng, 4D printing Light-Driven soft actuators based on Liquid-Vapor phase transition composites with inherent sensing capability, Chemical Engineering Journal 454 (2023) 140271. doi:10.1016/j.cej.2022.140271.

[4] X. Xu, J. Cheng, H. Zhao, W. He, L. Zhang, Z. Cheng, Second-Generation Soft Actuators Driven by NIR Light Based on Croconaine

Dye-Doped Vitrimers, ACS Applied Materials & Interfaces 15 (2023) 41916–41926. doi:10.1021/acsami.3c08973.

[5] V. H. Nguyen, S. Oh, M. Mahato, R. Tabassian, H. Yoo, S.-G. Lee, M. Garai, K. J. Kim, I.-K. Oh, Functionally antagonistic polyelectrolyte for electro-ionic soft actuator, Nature Communications 15 (2024) 435. doi:10.1038/s41467-024-44719-z.

[6] H. Zhang, S. Huang, J. Sheng, C. Wang, J. Zhang, M. Zhu, Emmanuel. Agyenim-Boateng, C. Liang, B. Xue, H. Yang, J. Zhou, J. Lu, Regulation of electrically responsive shape recovery behavior of 4D printed polymers for application in actuators, Additive Manufacturing 78 (2023) 103836. doi:10.1016/j.addma.2023.103836.

[7] J. Bernat, P. Gajewski, J. Kołota, A. Marcinkowska, Review of Soft Actuators Controlled with Electrical Stimuli: IPMC, DEAP, and MRE, Applied Sciences 13 (2023) 1651. doi:10.3390/app13031651.

[8] Z. Wang, Y. Wu, B. Zhu, Q. Chen, L. Wang, Y. Zhao, D. Sun, J. Zheng, D. Wu, A magnetic soft robot with multimodal sensing capability by multimaterial direct ink writing, Additive Manufacturing 61 (2023) 103320. doi:10.1016/j.addma.2022.103320.

[9] M. Richter, J. Sikorski, P. Makushko, Y. Zabila, V. K. Venkiteswaran, D. Makarov, S. Misra, Locally Addressable Energy Efficient Actuation of Magnetic Soft Actuator Array Systems, Advanced Science 10 (2023) 2302077. doi:10.1002/advs.202302077.

[10] G. Chen, T. Lin, G. Lodewijks, A. Ji, Design of an Active Flexible Spine for Wall Climbing Robot Using Pneumatic Soft Actuators, Journal of Bionic Engineering 20 (2023) 530–542. doi:10.1007/s42235-022-00273-2.

[11] J. Wu, W. Ai, Y. Long, K. Song, MXene-Based Soft Humidity-Driven Actuator with High Sensitivity and Fast Response, ACS Applied Materials & Interfaces 16 (2024) 27650–27656. doi:10.1021/acsami.4c04111.

[12] R. Lan, W. Shen, W. Yao, J. Chen, X. Chen, H. Yang, Bioinspired humidity-responsive liquid crystalline materials: From adaptive soft actuators to visualized sensors and detectors, Materials Horizons 10 (2023) 2824–2844. doi:10.1039/D3MH00392B.

[13] T. Hanuhov, N. Cohen, Design principles for 3D-printed thermally activated shape-morphing structures, International Journal of Mechanical Sciences 262 (2024) 108716. doi:10.1016/j.ijmecsci.2023.108716.

[14] T. Gu, H. Bi, H. Sun, J. Tang, Z. Ren, X. Zhou, M. Xu, Design and development of 4D-printed cellulose nanofibers reinforced shape memory polymer composites: Application for self-deforming plant bionic soft grippers, Additive Manufacturing 70 (2023) 103544. doi:10.1016/j.addma.2023.103544.

[15] B. Zhou, M. A. Aouraghe, W. Chen, Q. Jiang, F. Xu, Highly Responsive Soft Electrothermal Actuator with High-Output Force Based on Polydimethylsiloxane (PDMS)-Coated Carbon Nanotube

(CNT) Sponge, Nano Letters 23 (2023) 6504–6511. doi:10.1021/acs.nanolett.3c01458.

[16] G. Fusi, D. Del Giudice, O. Skarsetz, S. Di Stefano, A. Walther, Autonomous Soft Robots Empowered by Chemical Reaction Networks, Advanced Materials 35 (2023) 2209870. doi:10.1002/adma.202209870.

[17] C. Lin, X. Xin, L. Tian, D. Zhang, L. Liu, Y. Liu, J. Leng, Thermal-, magnetic-, and light-responsive 4D printed SMP composites with multiple shape memory effects and their promising applications, Composites Part B: Engineering 274 (2024) 111257. doi:10.1016/j.compositesb.2024.111257.

[18] F. Peng, Y. Song, T. Xu, M. Wang, N. Song, S. Sun, P. Ding, Smart polymer composites with vertically oriented boron nitride and carbon fiber for heat management: Magneto-thermal responsiveness, Composites Part B: Engineering 283 (2024) 111617. doi:10.1016/j.compositesb.2024.111617.

[19] J. Ahn, J. Gu, J. Choi, C. Han, Y. Jeong, J. Park, S. Cho, Y. S. Oh, J.-H. Jeong, M. Amjadi, I. Park, A Review of Recent Advances in Electrically Driven Polymer-Based Flexible Actuators: Smart Materials, Structures, and Their Applications, Advanced Materials Technologies 7 (2022) 2200041. doi:10.1002/admt.202200041.

[20] L. Yang, H. Wang, High-performance electrically responsive artificial muscle materials for soft robot actuation, Acta Biomaterialia 185 (2024) 24–40. doi:10.1016/j.actbio.2024.07.016.

[21] W. Sun, H. Liang, F. Zhang, H. Wang, Y. Lu, B. Li, G. Chen, Dielectric elastomer minimum energy structure with a unidirectional actuation for a soft crawling robot: Design, modeling, and kinematic study, International Journal of Mechanical Sciences 238 (2023) 107837. doi:10.1016/j.ijmecsci.2022.107837.

[22] D. Wang, B. Zhao, X. Li, L. Dong, M. Zhang, J. Zou, G. Gu, Dexterous electrical-driven soft robots with reconfigurable chiral-lattice foot design, Nature Communications 14 (2023) 5067. doi:10.1038/s41467-023-40626-x.

[23] H. Zhang, X. Yang, C. Valenzuela, Y. Chen, Y. Yang, S. Ma, L. Wang, W. Feng, Wireless Power Transfer to Electrothermal Liquid Crystal Elastomer Actuators, ACS Applied Materials & Interfaces 15 (2023) 27195–27205. doi:10.1021/acsami.3c03817.

[24] Y. Wang, T. Guo, Z. Tian, L. Shi, S. C. Barman, H. N. Alshareef, MXenes for soft robotics, Matter 6 (2023) 2807–2833. doi:10.1016/j.matt.2023.07.013.

[25] Y. Zhao, Z. Liu, C. Li, W. Jiao, S. Jiang, X. Li, J. Duan, J. Li, Mechanically reconfigurable metasurfaces: Fabrications and applications, npj Nanophotonics 1 (2024) 16. doi:10.1038/s44310-024-00010-z.

[26] Z. Wang, S. Wang, Z. Du, L. Yang, X. Cheng, H. Wang, Multifunctional wearable electronic textile based on fabric modified by MXene/Ag NWs for pressure sensing, EMI and personal thermal

management, Composites Part B: Engineering 266 (2023) 110999. doi:10.1016/j.compositesb.2023.110999.

[27] Y. Lv, Q. Wei, L. Ye, Y. Huang, L. Zhang, R. Shen, Z. Li, S. Lu, Liquid metal flexible multifunctional sensors with ultra-high conductivity for use as wearable sensors, joule heaters and electromagnetic shielding materials, Composites Part B: Engineering 291 (2025) 112064. doi:10.1016/j.compositesb.2024.112064.

[28] Y. Tian, Y.-T. Li, H. Tian, Y. Yang, T.-L. Ren, Recent Progress of Soft Electrothermal Actuators, Soft Robotics 8 (2021) 241–250. doi:10.1089/soro.2019.0164.

[29] D. C. Nguyen, T. D. Nguyen, Y. S. Kim, Highly affordable electrothermal actuators based on an embedded Cu microheater with a high-resolution pattern, Sensors and Actuators A: Physical 372 (2024) 115333. doi:10.1016/j.sna.2024.115333.

[30] Potekhina, Wang, Review of Electrothermal Actuators and Applications, Actuators 8 (2019) 69. doi:10.3390/act8040069.

[31] C. Fang, B. Xu, M. Li, J. Han, Y. Yang, X. Liu, Advanced Design of Fibrous Flexible Actuators for Smart Wearable Applications, Advanced Fiber Materials 6 (2024) 622–657. doi:10.1007/s42765-024-00386-9.

[32] Y. Tian, M. Dong, X. Wang, Y. Zhou, J. Qian, Fully Handwritten Flexible Electrothermal Devices Using a Whiteboard Marker Pen with Carbon Nanoparticle Ink, ACS Applied Electronic Materials 6 (2024) 4288–4296. doi:10.1021/acsaelm.4c00375.

[33] H. Wang, X. Li, X. Wang, Y. Qin, Y. Pan, X. Guo, Somatosensory Electro-Thermal Actuator through the Laser-Induced Graphene Technology, Small 20 (2024) 2310612. doi:10.1002/smll.202310612.

[34] A. Pimpin, W. Srituravanich, G. Phanomchoeng, N. Damrongplasit, Position Feedback-Control of an Electrothermal Microactuator Using Resistivity Self-Sensing Technique, Sensors 24 (2024) 3328. doi:10.3390/s24113328.

[35] C. Liu, J. Luo, H. Liu, J. Fu, H. Liu, H. Tang, Z. Deng, J. Wu, Y. Li, C. Liu, S. Peng, J. Hu, T.-L. Ren, J. Zhou, Y. Qiao, Intelligent Soft Quasi-Organism Equipped with Sensor-Driven Integrated Tentacles, Advanced Functional Materials (2024) 2404333. doi:10.1002/adfm.202404333.

[36] Z. Zhang, F. Bu, E. Cheng, C. Yang, Z. Zhang, N. Hu, Lower-Voltage-Driven Deformable Soft Electrothermal Actuators with Embedded Liquid Metal EGaIn, Advanced Engineering Materials (2023) 2300253. doi:10.1002/adem.202300253.

[37] A. Zolfagharian, S. Gharaie, A. Z. Kouzani, M. Lakhi, S. Ranjbar, M. Lalegani Dezaki, M. Bodaghi, Silicon-based soft parallel robots 4D printing and multiphysics analysis, Smart Materials and Structures 31 (2022) 115030. doi:10.1088/1361-665X/ac976c.

[38] Z. Huo, J. He, H. Pu, J. Luo, D. Li, Design and printing of embedded conductive patterns in liquid crystal elastomer for programmable

electrothermal actuation, Virtual and Physical Prototyping 17 (2022) 881–893. doi:10.1080/17452759.2022.2087096.

[39] W. Qiu, X. Xu, K. Dong, Y. Wang, Y. Xiong, Recent advances in 4D printing of fiber-reinforced polymer composites: A review and outlook, Composites Part B: Engineering 283 (2024) 111645. doi:10.1016/j.compositesb.2024.111645.

[40] S. Kashef Tabrizian, W. Alabiso, U. Shaukat, S. Terryn, E. Rossegger, J. Brancart, J. Legrand, S. Schlögl, B. Vanderborght, Vitrimeric shape memory polymer-based fingertips for adaptive grasping, Frontiers in Robotics and AI 10 (2023) 1206579. doi:10.3389/frobt.2023.1206579.

[41] F. Daniel, J. Fontenot, A. D. Radadia, Characterization of an electrothermal gripper fabricated via extrusion-based additive manufacturing, Sensors and Actuators A: Physical 333 (2022) 113302. doi:10.1016/j.sna.2021.113302.

[42] Z. Jiang, B. Diggle, M. L. Tan, J. Viktorova, C. W. Bennett, L. A. Connal, Extrusion 3D Printing of Polymeric Materials with Advanced Properties, Advanced Science 7 (2020) 2001379. doi:10.1002/advs.202001379.

[43] H. Ren, X. Yang, Z. Wang, X. Xu, R. Wang, Q. Ge, Y. Xiong, Smart structures with embedded flexible sensors fabricated by fused deposition modeling-based multimaterial 3D printing, International Jour-

nal of Smart and Nano Materials 13 (2022) 447–464. doi:10.1080/19475411.2022.2095454.

[44] T. B. Palmić, J. Slavič, Design principles for a single-process 3D-printed stacked dielectric actuators — Theory and experiment, International Journal of Mechanical Sciences 246 (2023) 108128. doi:10.1016/j.ijmecsci.2023.108128.

[45] T. Košir, J. Slavič, Manufacturing of single-process 3D-printed piezoelectric sensors with electromagnetic protection using thermoplastic material extrusion, Additive Manufacturing 73 (2023) 103699. doi:10.1016/j.addma.2023.103699.

[46] M. Arh, J. Slavič, Single-Process 3D-Printed Triaxial Accelerometer, Advanced Materials Technologies 7 (2022) 2101321. doi:10.1002/admt.202101321.

[47] T. Košir, M. Zupan, J. Slavič, Self-aware active metamaterial cell 3D-printed in a single process, International Journal of Mechanical Sciences 282 (2024) 109591. doi:10.1016/j.ijmecsci.2024.109591.

[48] C.-T. Chen, R.-C. Peng, Design and 3D printing of paper-based shape memory polymer actuated for soft lightweight fingers, Smart Materials and Structures 30 (2021) 075010. doi:10.1088/1361-665X/ac00ca.

[49] G. Duan, H. Liu, Z. Liu, J. Tan, A 4D-Printed Structure With Reversible Deformation for the Soft Crawling Robot, Frontiers in Materials 9 (2022) 850722. doi:10.3389/fmats.2022.850722.

[50] C.-T. Chen, P.-S. Liao, Additive design and manufacturing of a quadruped robot actuated by electrothermal effect of shape memory polymer, Sensors and Actuators A: Physical 357 (2023) 114401. doi:10.1016/j.sna.2023.114401.

[51] Y. C. Lee, Y. S. Alshebly, M. Nafea, Joule Heating Activation of 4D Printed Conductive PLA Actuators, in: 2022 IEEE International Conference on Automatic Control and Intelligent Systems (I2CACIS), IEEE, Shah Alam, Malaysia, 2022, pp. 221–225. doi:10.1109/I2CACIS54679.2022.9815495.

[52] R. Delbart, C. Robert, T. Truong Hoang, F. Martinez-Hergueta, Development of an electro-thermo-mechanical 4D printed multi-shape smart actuator: Experiments and simulation, Composites Part A: Applied Science and Manufacturing 186 (2024) 108381. doi:10.1016/j.compositesa.2024.108381.

[53] Jian Jiao, Yuan Guo, Qianqian Tong, Shengkai Liu, Pengfei Qiu, Tao Mei, Dangxiao Wang, Stiffness-tunable and shape-locking soft actuators based on 3D-printed hybrid multi-materials, Soft Science 2 (2022) 20. doi:10.20517/ss.2022.19.

[54] C.-T. Chen, Z.-L. Chen, Direct ink writing of polymer matrix composite with carbon for driving a flexible thermoelectric actuator of shape memory polymer, Materials Today Communications 38 (2024) 108303. doi:10.1016/j.mtcomm.2024.108303.

[55] W.-C. Chen, C.-C. Chu, J. Hsieh, W. Fang, A reliable single-layer

out-of-plane micromachined thermal actuator, Sensors and Actuators A: Physical 103 (2003) 48–58. doi:10.1016/S0924-4247(02)00315-1.

[56] Y. Liu, Q. Gan, S. Baig, E. Smela, Improving adhesion of polypyrrole to gold for long-term actuation, in: Y. Bar-Cohen (Ed.), Smart Structures and Materials, San Diego, CA, 2005, p. 396. doi:10.1117/12.599753.

[57] B. Shapiro, E. Smela, Bending Actuators with Maximum Curvature and Force and Zero Interfacial Stress, Journal of Intelligent Material Systems and Structures 18 (2007) 181–186. doi:10.1177/1045389X06063801.

[58] S. Delia, A. Rochman, A. Curmi, Factors affecting interface bonding in multi-material additive manufacturing, Progress in Additive Manufacturing 9 (2024) 1365–1379. doi:10.1007/s40964-024-00617-w.

[59] G. L. Goh, S. Lee, S. H. Cheng, D. J. S. Goh, P. Laya, V. P. Nguyen, B. S. Han, W. Y. Yeong, Enhancing interlaminar adhesion in multi-material 3D printing: A study of conductive PLA and TPU interfaces through fused filament fabrication, Materials Science in Additive Manufacturing 3 (2024) 2672. doi:10.36922/msam.2672.

[60] Y. A. AboZaid, M. T. Aboelrayat, I. S. Fahim, A. G. Radwan, Soft robotic grippers: A review on technologies, materials, and applications, Sensors and Actuators A: Physical 372 (2024) 115380. doi:10.1016/j.sna.2024.115380.

[61] Y. Hao, Z. Liu, J. Liu, X. Fang, B. Fang, S. Nie, Y. Guan, F. Sun, T. Wang, L. Wen, A soft gripper with programmable effective length,

tactile and curvature sensory feedback, Smart Materials and Structures 29 (2020) 035006. doi:10.1088/1361-665X/ab6759.

[62] G. L. Goh, G. D. Goh, V. P. Nguyen, W. Toh, S. Lee, X. Li, B. D. Sunil, J. Y. Lim, Z. Li, A. K. Sinha, W. Y. Yeong, D. Campolo, W. T. Chow, T. Y. Ng, B. S. Han, A 3D Printing-Enabled Artificially Innervated Smart Soft Gripper with Variable Joint Stiffness, Advanced Materials Technologies 8 (2023) 2301426. doi:10.1002/admt.202301426.

[63] R. Nam, J. E. Lee, M. Jakubinek, B. Ashrafi, H. E. Naguib, Soft electrothermal actuator array for surface morphing application, MRS Bulletin 48 (2023) 819–827. doi:10.1557/s43577-022-00474-4.

[64] A. Montazeri, M. Naderinejad, M. Mahnama, A. Hasani, 3D-Printed Twisting Tubular Metamaterials with Tunable Mechanical and Torsional Characteristics, International Journal of Mechanical Sciences 262 (2024) 108719. doi:10.1016/j.ijmecsci.2023.108719.

[65] P. Xu, X. Lan, C. Zeng, X. Zhang, H. Zhao, J. Leng, Y. Liu, Compression behavior of 4D printed metamaterials with various Poisson's ratios, International Journal of Mechanical Sciences 264 (2024) 108819. doi:10.1016/j.ijmecsci.2023.108819.

[66] Q. Zhang, Y. Sun, Novel metamaterial structures with negative thermal expansion and tunable mechanical properties, International Journal of Mechanical Sciences 261 (2024) 108692. doi:10.1016/j.ijmecsci.2023.108692.

[67] H. Hussein, H. Fariborzi, M. I. Younis, Modeling of Beam Electrothermal Actuators, Journal of Microelectromechanical Systems 29 (2020) 1570–1581. doi:10.1109/JMEMS.2020.3033477.

[68] Y. Cao, J. Dong, Self-Sensing and Control of Soft Electrothermal Actuator, IEEE/ASME Transactions on Mechatronics 26 (2021) 854–863. doi:10.1109/TMECH.2020.3009237.

[69] G. Krivic, J. Slavič, Simultaneous non-contact identification of the elastic modulus, damping and coefficient of thermal expansion in 3D-printed structures, Polymer Testing 125 (2023) 108131. doi:10.1016/j.polymertesting.2023.108131.

[70] E. Wojtczak, M. Rucka, A. Andrzejewska, A procedure for the identification of effective mechanical parameters of additively manufactured elements using integrated ultrasonic bulk and guided waves, Measurement 231 (2024) 114628. doi:10.1016/j.measurement.2024.114628.

[71] A. Bertocco, M. Bruno, E. Armentani, L. Esposito, M. Perrella, Stress Relaxation Behavior of Additively Manufactured Polylactic Acid (PLA), Materials 15 (2022) 3509. doi:10.3390/ma15103509.

[72] K. Tüfekci, B. G. Çakan, V. M. Küçükakarsu, Stress relaxation of 3D printed PLA of various infill orientations under tensile and bending loadings, Journal of Applied Polymer Science 140 (2023) e54463. doi:10.1002/app.54463.

[73] V. M. Bruère, A. Lion, J. Holtmannspötter, M. Johlitz, The influence of printing parameters on the mechanical properties of 3D printed TPU-

based elastomers, Progress in Additive Manufacturing 8 (2023) 693–701. doi:10.1007/s40964-023-00418-7.

[74] S. Timoshenko, Analysis of Bi-Metal Thermostats, Journal of the Optical Society of America 11 (1925) 233. doi:10.1364/JOSA.11.000233.

[75] P. Du, X. Lin, X. Zhang, A multilayer bending model for conducting polymer actuators, Sensors and Actuators A: Physical 163 (2010) 240–246. doi:10.1016/j.sna.2010.06.002.

[76] W.-H. Chu, M. Mehregany, R. L. Mullen, Analysis of tip deflection and force of a bimetallic cantilever microactuator, Journal of Micromechanics and Microengineering 3 (1993) 4–7. doi:10.1088/0960-1317/3/1/002.

[77] S. Kim, K.-S. Kim, Y. Kim, Analytical modeling of Ni–Co based multilayer bimorph actuators involving dual insulation layers, Sensors and Actuators A: Physical 348 (2022) 113984. doi:10.1016/j.sna.2022.113984.

[78] G. Tibi, E. Sachyani Keneth, M. Layani, S. Magdassi, A. Degani, Three-Layered Design of Electrothermal Actuators for Minimal Voltage Operation, Soft Robotics 7 (2020) 649–662. doi:10.1089/soro.2018.0160.

[79] G. Tibi, E. Sachyani, M. Layani, S. Magdassi, A. Degani, Analytic modeling and experiments of tri-layer, electro-thermal actuators for thin and soft robotics, in: 2017 IEEE International Conference on

Robotics and Automation (ICRA), IEEE, Singapore, Singapore, 2017, pp. 6712–6717. doi:10.1109/ICRA.2017.7989794.

[80] S. Todd, Huikai Xie, An Electrothermomechanical Lumped Element Model of an Electrothermal Bimorph Actuator, Journal of Microelectromechanical Systems 17 (2008) 213–225. doi:10.1109/JMEMS.2007.908754.

[81] R. Torre, S. Brischetto, Experimental characterization and finite element validation of orthotropic 3D-printed polymeric parts, International Journal of Mechanical Sciences 219 (2022) 107095. doi:10.1016/j.ijmecsci.2022.107095.

[82] T. L. Bergman, A. S. Levine, Fundamentsl of Heat and Mass Transfer, eighth edition wiley loose-leaf print edition ed., John Wiley & Sons, Inc., Hoboken, NJ, 2019.

[83] S. Becker, S. Gutschmidt, B. Boyd, D. Zhao, Pulsed heating of the self-actuated cantilever: A one-dimensional exact solution investigation of non-axial temperature gradients, Journal of Engineering Mathematics 146 (2024) 9. doi:10.1007/s10665-024-10359-x.

[84] B. Apaçoğlu-Turan, K. Kırkköprü, M. Çakan, Numerical Modeling and Analysis of Transient and Three-Dimensional Heat Transfer in 3D Printing via Fused-Deposition Modeling (FDM), Computation 12 (2024) 27. doi:10.3390/computation12020027.

[85] N. Mosleh, M. Esfandeh, S. Dariushi, Simulation of temperature profile

in fused filament fabrication 3D printing method, Rapid Prototyping Journal 30 (2024) 134–144. doi:10.1108/RPJ-02-2023-0067.

[86] P. Scherz, S. Monk, Practical Electronics for Inventors, fourth edition ed., McGraw Hill Education, New York Chicago San Francisco Athens London, 2016.

[87] F. Hong, B. Lampret, C. Myant, S. Hodges, D. Boyle, 5-axis multi-material 3D printing of curved electrical traces, Additive Manufacturing 70 (2023) 103546. doi:10.1016/j.addma.2023.103546.

[88] F. Aliberti, A. Sorrentino, B. Palmieri, L. Vertuccio, G. De Tommaso, R. Pantani, L. Guadagno, A. Martone, Lightweight 3D-printed heaters: Design and applicative versatility, Composites Part C: Open Access 15 (2024) 100527. doi:10.1016/j.jcomc.2024.100527.

[89] A. Steckiewicz, K. Konopka, A. Choroszucho, J. M. Stankiewicz, Temperature Measurement at Curved Surfaces Using 3D Printed Planar Resistance Temperature Detectors, Electronics 10 (2021) 1100. doi:10.3390/electronics10091100.

[90] A. M. L. Lanzolla, F. Attivissimo, G. Percoco, M. A. Ragolia, G. Stano, A. Di Nisio, Additive Manufacturing for Sensors: Piezoresistive Strain Gauge with Temperature Compensation, Applied Sciences 12 (2022) 8607. doi:10.3390/app12178607.

[91] M. J. Hossain, B. T. Tabatabaei, M. Kiki, J.-W. Choi, Additive Manufacturing of Sensors: A Comprehensive Review, International Jour-

nal of Precision Engineering and Manufacturing-Green Technology 12 (2025) 277–300. doi:10.1007/s40684-024-00629-5.

[92] S. R. Rajpurohit, H. K. Dave, M. Bodaghi, Classical laminate theory for flexural strength prediction of FDM 3D printed PLAs, Materials Today: Proceedings (2023) S2214785323013561. doi:10.1016/j.matpr.2023.03.310.

[93] F. Medel, J. Abad, V. Esteban, Stiffness and damping behavior of 3D printed specimens, Polymer Testing 109 (2022) 107529. doi:10.1016/j.polymertesting.2022.107529.

[94] C. Casavola, A. Cazzato, V. Moramarco, C. Pappalettere, Orthotropic mechanical properties of fused deposition modelling parts described by classical laminate theory, Materials & Design 90 (2016) 453–458. doi:10.1016/j.matdes.2015.11.009.

[95] G. H. Staab, Laminar Composites, second edition ed., Butterworth-Heinemann, Amsterdam ; Boston, MA, 2015.

[96] R. C. Hibbeler, Mechanics of Materials, tenth edition in si units, global edition ed., Pearson, Harlow, 2018.

[97] R. S. Lakes, Viscoelastic Materials, Cambridge University Press, Cambridge ; New York, 2009.

[98] H. E. Pettermann, A. DeSimone, An anisotropic linear thermo-viscoelastic constitutive law: Elastic relaxation and thermal expansion creep in the time domain, Mechanics of Time-Dependent Materials 22 (2018) 421–433. doi:10.1007/s11043-017-9364-x.

[99] B. Fazekas, T. J. Goda, Constitutive modelling of rubbers: Mullins effect, residual strain, time-temperature dependence, International Journal of Mechanical Sciences 210 (2021) 106735. doi:10.1016/j.ijmecsci.2021.106735.

[100] S. Huang, Y. Qi, J. Zhang, B. Gu, B. Sun, Multiscale homogenization of thermo-mechanical viscoelastic response of 3D orthogonal composites with time-dependent CTEs, Composite Structures 347 (2024) 118479. doi:10.1016/j.compstruct.2024.118479.

[101] W. Cai, P. Wang, Fractional modeling of temperature-dependent mechanical behaviors for glassy polymers, International Journal of Mechanical Sciences 232 (2022) 107607. doi:10.1016/j.ijmecsci.2022.107607.

[102] M. Arh, J. Slavič, M. Boltežar, Experimental identification of the dynamic piezoresistivity of fused-filament-fabricated structures, Additive Manufacturing 36 (2020) 101493. doi:10.1016/j.addma.2020.101493.

[103] F. Suárez-Carreño, L. Rosales-Romero, Convergency and Stability of Explicit and Implicit Schemes in the Simulation of the Heat Equation, Applied Sciences 11 (2021) 4468. doi:10.3390/app11104468.

[104] S. W. Churchill, H. H. Chu, Correlating equations for laminar and turbulent free convection from a vertical plate, International Journal of Heat and Mass Transfer 18 (1975) 1323–1329. doi:10.1016/0017-9310(75)90243-4.

[105] A. R. Ghasemi, A. Tabatabaeian, A unified comparative study on the classical lamination theory, hole drilling, slitting, and curvature measurement methods for assessment of residual stress in laminated polymeric composites, Mechanics of Materials 167 (2022) 104267. doi:10.1016/j.mechmat.2022.104267.

[106] Ç. Yılmaz, H. Q. Ali, M. Yıldız, Monitoring and verification of micro-strain generated inside the laminate subjected to thermal loading through fiber bragg grating sensors and classical laminate theory, Polymer Composites 44 (2023) 2956–2965. doi:10.1002/pc.27293.

[107] P. Cortés, W. Cantwell, The prediction of tensile failure in titanium-based thermoplastic fibre–metal laminates, Composites Science and Technology 66 (2006) 2306–2316. doi:10.1016/j.compscitech.2005.11.031.

[108] ISO 527-1:2019, Plastics — Determination of tensile properties, 2019.

[109] C. Tzikang, Determining a Prony Series for a Viscoelastic Material from Time Varying Strain Data, Technical Report NASA/TM-2000-210123 ARL-TR-2206, National Aeronautics and Space Administration, 2000.

[110] Nur Izzi Md. Yusoff, Emmanuel Chailleux, Gordon D. Airey, A Comparative Study of the Influence of Shift Factor Equations on Master Curve Construction, International Journal of Pavement Research and Technology 4 (2011). doi:10.6135/ijprt.org.tw/2011.4(6).324.

Appendix A. Classical Lamination Theory

The Classical Lamination Theory presented here is applicable to orthotropic thin laminates, where the strain variation through the laminate is described by the mid-surface strains $\{\boldsymbol{\varepsilon^0}\}$ and the mid-surface curvatures $\{\boldsymbol{\kappa}\}$ (Fig. A.9a) [92, 93, 94, 95]:

$$\begin{Bmatrix} \varepsilon_x \\ \varepsilon_y \\ \varepsilon_{xy} \end{Bmatrix} = \begin{Bmatrix} \varepsilon_x^0 \\ \varepsilon_y^0 \\ \varepsilon_{xy}^0 \end{Bmatrix} + z \begin{Bmatrix} \kappa_x \\ \kappa_y \\ \kappa_{xy} \end{Bmatrix}, \tag{A.1}$$

where the z coordinate runs through the thickness of the laminate, starting at the mid-surface, as shown in Fig. A.9b.

Assuming linear elastic material properties and a plane stress stress-strain relationship, the stress in the k-th lamina is given by [92, 93, 94, 95]:

$$\begin{Bmatrix} \sigma_x \\ \sigma_y \\ \sigma_{xy} \end{Bmatrix}_k = \left[\overline{\mathbf{Q}}\right]_k \left(\begin{Bmatrix} \varepsilon_x^0 \\ \varepsilon_y^0 \\ \varepsilon_{xy}^0 \end{Bmatrix} + z \begin{Bmatrix} \kappa_x \\ \kappa_y \\ \kappa_{xy} \end{Bmatrix} \right), \tag{A.2}$$

where $\left[\overline{\mathbf{Q}}\right]_k$ is the in-plane stiffness matrix of the k-th lamina. The in-plane stiffness matrix $\left[\overline{\mathbf{Q}}\right]_k$ is obtained by transforming the stiffness matrix in the principal coordinate system $[\mathbf{Q}]_k$ to the Cartesian coordinate system [93, 95]:

$$\left[\overline{\mathbf{Q}}\right]_k = [\mathbf{T}_{\boldsymbol{\sigma}}]_k^{-1} \, [\mathbf{Q}]_k \, [\mathbf{T}_{\boldsymbol{\varepsilon}}]_k . \tag{A.3}$$

Here, $[\mathbf{T}_{\boldsymbol{\sigma}}]_k$ and $[\mathbf{T}_{\boldsymbol{\varepsilon}}]_k$ are the off-axis transformation matrices, defined as [93,

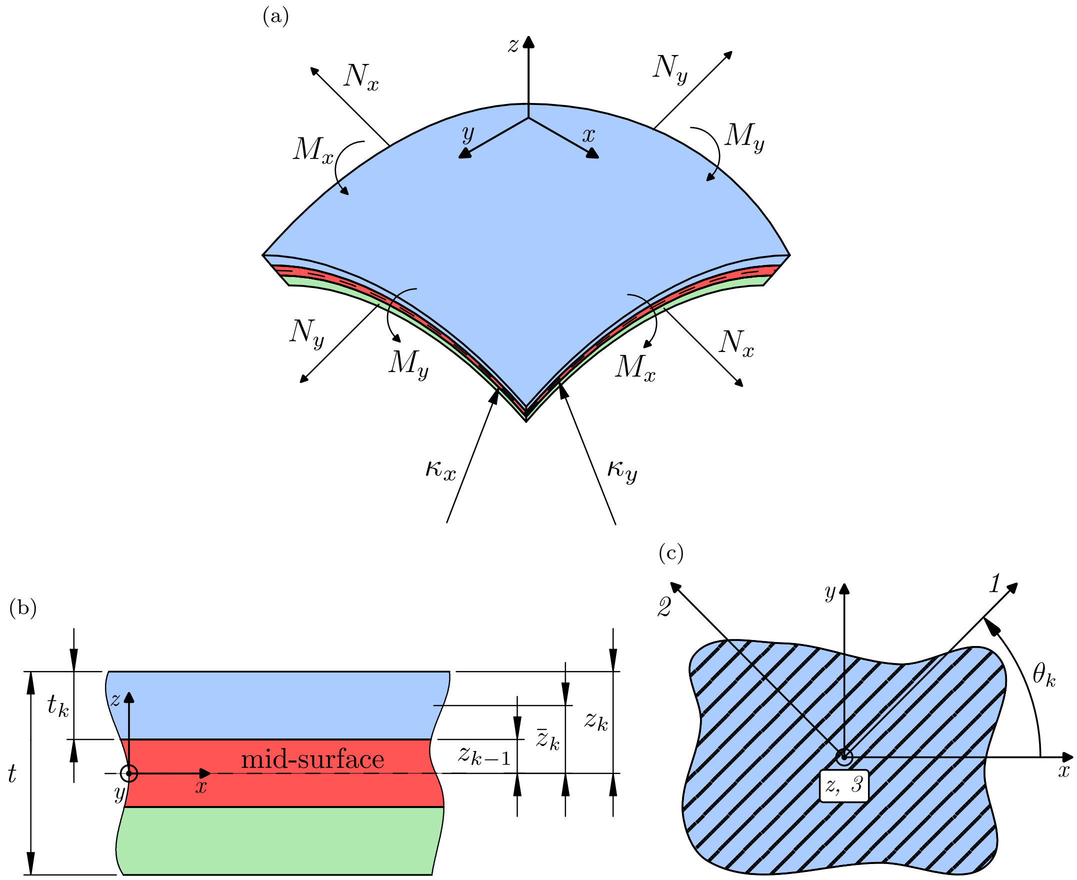

Figure A.9: (a) Schematic illustration of a laminate with mid-surface curvatures $\{\boldsymbol{\kappa}\}$ and mechanical loads and moments ($\{\mathbf{N}\}$ and $\{\mathbf{M}\}$). (b) Cross-sectional view showing the total thickness t, divided among individual laminae. (c) Fiber orientation in each lamina, with principal material axes defined relative to the x-axis by the angle θ_k.

95]:

$$[\mathbf{T}_{\boldsymbol{\sigma}}]_k = \begin{bmatrix} m^2 & n^2 & 2m\,n \\ n^2 & m^2 & -2m\,n \\ -m\,n & m\,n & m^2-n^2 \end{bmatrix},\ [\mathbf{T}_{\boldsymbol{\varepsilon}}]_k = \begin{bmatrix} m^2 & n^2 & m\,n \\ n^2 & m^2 & -m\,n \\ -2m\,n & 2m\,n & m^2-n^2 \end{bmatrix}, \tag{A.4}$$

where $m = \cos\theta_k$ and $n = \sin\theta_k$, with θ_k being the angle measured from the x-axis to the 1st principal axis of the k-th lamina, as shown in Fig A.9c.

The in-plane stiffness matrix for plane stress inthe principal coordinate system has the following form [92, 93, 94, 95]:

$$[\mathbf{Q}]_k = \begin{bmatrix} Q_{11} & Q_{12} & 0 \\ Q_{12} & Q_{22} & 0 \\ 0 & 0 & Q_{66} \end{bmatrix}, \tag{A.5}$$

where the individual terms are [92, 93, 94, 95]:

$$Q_{11} = \frac{E_1^2}{E_1 - \nu_{12}^2 E_2},\ Q_{22} = \frac{E_1\, E_2}{E_1 - \nu_{12}^2 E_2},\ Q_{12} = \frac{\nu_{12} E_1\, E_2}{E_1 - \nu_{12}^2 E_2},\ Q_{66} = G_{12}. \tag{A.6}$$

Here, E_i is the elastic modulus along the i-th principal axis, ν_{12} is Poissons's ratio in the 2nd direction when a load is applied along the 1st principal axis, and G_{12} is the shear modulus corresponding to shear stress applied to the 12-plane. The following relationship is also considered in Eq. (A.6): $\nu_{12}/E_1 = \nu_{21}/E_2$ [92, 93, 94, 95].

The laminate loads are assumed to consist of resultant forces $\{\mathbf{N}\}$ and moments $\{\mathbf{M}\}$, defined for a representative section of the laminate in Fig. A.9b. The resultant forces have units of force per unit length of the laminate (N/m), while the resultant moments have units of force times length per unit length of the laminate (N m/m). To satisfy equilibrium conditions, the resultant laminate forces and moments must be balanced by the integral of stresses over the laminate thickness, leading to the following relationship [92, 95]:

$$\{\mathbf{N}\} = \begin{Bmatrix} N_x \\ N_y \\ N_{xy} \end{Bmatrix} = \int_{-t/2}^{t/2} \begin{Bmatrix} \sigma_x \\ \sigma_y \\ \sigma_{xy} \end{Bmatrix} \mathrm{d}z = \sum_{k=1}^{N} \int_{z_{k-1}}^{z_k} \begin{Bmatrix} \sigma_x \\ \sigma_y \\ \sigma_{xy} \end{Bmatrix}_k \mathrm{d}z, \tag{A.7}$$

$$\{\mathbf{M}\} = \begin{Bmatrix} M_x \\ M_y \\ M_{xy} \end{Bmatrix} = \int_{-t/2}^{t/2} z \begin{Bmatrix} \sigma_x \\ \sigma_y \\ \sigma_{xy} \end{Bmatrix} \mathrm{d}z = \sum_{k=1}^{N} \int_{z_{k-1}}^{z_k} z \begin{Bmatrix} \sigma_x \\ \sigma_y \\ \sigma_{xy} \end{Bmatrix}_k \mathrm{d}z, \tag{A.8}$$

where t is the thickness of the laminate, N is the number of lamina, and the k-th lamina has bottom and top z-coordinates of z_{k-1} and z_k, respectively (see Fig. A.9b).

Substituting Eq. (A.2) into Eqs. (A.7) and (A.8), and considering that the mid-surface strains $\{\boldsymbol{\varepsilon}^{\mathbf{0}}\}$ and curvatures $\{\boldsymbol{\kappa}\}$ are independent of the z-coordinate, the integration is simplified. The loads and moments can be expressed in matrix form, after integration, as [92, 94, 95]:

$$\begin{Bmatrix} \{\mathbf{N}\} \\ \{\mathbf{M}\} \end{Bmatrix} = \begin{bmatrix} [\mathbf{A}] & [\mathbf{B}] \\ [\mathbf{B}] & [\mathbf{D}] \end{bmatrix} \begin{Bmatrix} \{\boldsymbol{\varepsilon}^{\mathbf{0}}\} \\ \{\boldsymbol{\kappa}\} \end{Bmatrix}, \tag{A.9}$$

where matrix $[\mathbf{A}]$ is the extensional stiffness matrix, $[\mathbf{B}]$ is the extension-bending coupling matrix, and $[\mathbf{D}]$ is the bending stiffness matrix [92, 95]. The components of $[\mathbf{A}]$, $[\mathbf{B}]$, and $[\mathbf{D}]$ are defined as [92, 94, 95]:

$$[A_{ij}] = \sum_{k=1}^{N} \left[\overline{Q}_{ij}\right]_k t_k, \tag{A.10}$$

$$[B_{ij}] = \sum_{k=1}^{N} \left[\overline{Q}_{ij}\right]_k t_k\, \bar{z}_k, \tag{A.11}$$

$$[D_{ij}] = \sum_{k=1}^{N} \left[\overline{Q}_{ij}\right]_k \left(t_k\, \bar{z}_k^2 + \frac{t_k^3}{12} \right). \tag{A.12}$$

Here, the subscripts i and j refer to matrix indices, $t_k = z_k - z_{k-1}$ is the thickness of the k-th lamina, and $\bar{z}_k = (z_k + z_{k-1})/2$ is the location of the centroid of the k-th lamina from the mid-plane of the laminate (see Fig. A.9b).

For laminates with different thermal expansion properties among the laminae, thermal effects can result in significant residual strains and curvatures [95, 105, 106, 107]. Each lamina is constrained to deform with adjacent laminae, resulting in a uniform strain and curvature but differing residual stresses in each layer. The resulting laminate thermal loads $\left\{\mathbf{N}^{\mathrm{T}}\right\}$ and moments $\left\{\mathbf{M}^{\mathrm{T}}\right\}$ are defined as [95, 105, 106, 107]:

$$\begin{aligned} \left\{\mathbf{N}^{\mathbf{T}}\right\} = \begin{Bmatrix} N_x^{\mathrm{T}} \\ N_y^{\mathrm{T}} \\ N_{xy}^{\mathrm{T}} \end{Bmatrix} = \int_{-t/2}^{t/2} \begin{Bmatrix} \sigma_x^{\mathrm{T}} \\ \sigma_y^{\mathrm{T}} \\ \sigma_{xy}^{\mathrm{T}} \end{Bmatrix}_k \mathrm{d}z &= \int_{-t/2}^{t/2} \left[\overline{\mathbf{Q}}\right]_k \left[\mathbf{T}_{\boldsymbol{\varepsilon}}\right]_k^{-1} \begin{Bmatrix} \alpha_1 \\ \alpha_2 \\ 0 \end{Bmatrix}_k \Delta T \, \mathrm{d}z \\ &= \sum_{k=1}^{N} \left[\overline{\mathbf{Q}}\right]_k \left[\mathbf{T}_{\boldsymbol{\varepsilon}}\right]_k^{-1} \begin{Bmatrix} \alpha_1 \\ \alpha_2 \\ 0 \end{Bmatrix}_k \Delta T t_k, \end{aligned} \tag{A.13}$$

$$\begin{aligned} \left\{\mathbf{M}^{\mathbf{T}}\right\} = \begin{Bmatrix} M_x^{\mathrm{T}} \\ M_y^{\mathrm{T}} \\ M_{xy}^{\mathrm{T}} \end{Bmatrix} = \int_{-t/2}^{t/2} z \begin{Bmatrix} \sigma_x^{\mathrm{T}} \\ \sigma_y^{\mathrm{T}} \\ \sigma_{xy}^{\mathrm{T}} \end{Bmatrix}_k \mathrm{d}z &= \int_{-t/2}^{t/2} \left[\overline{\mathbf{Q}}\right]_k z \left[\mathbf{T}_{\boldsymbol{\varepsilon}}\right]_k^{-1} \begin{Bmatrix} \alpha_1 \\ \alpha_2 \\ 0 \end{Bmatrix}_k \Delta T \, \mathrm{d}z \\ &= \sum_{k=1}^{N} \left[\overline{\mathbf{Q}}\right]_k \left[\mathbf{T}_{\boldsymbol{\varepsilon}}\right]_k^{-1} \begin{Bmatrix} \alpha_1 \\ \alpha_2 \\ 0 \end{Bmatrix}_k \Delta T \, t_k \, \bar{z}_k, \end{aligned} \tag{A.14}$$

where α_i is the CTE along the i-th principal axis (see Fig. A.9c). Incorporating thermal loads and moments into Eq. (A.9) gives the following expression [95, 105]:

$$\begin{Bmatrix} \{\mathbf{N}\} \\ \{\mathbf{M}\} \end{Bmatrix} = \begin{bmatrix} [\mathbf{A}] & [\mathbf{B}] \\ [\mathbf{B}] & [\mathbf{D}] \end{bmatrix} \begin{Bmatrix} \{\boldsymbol{\varepsilon}^{\mathbf{0}}\} \\ \{\boldsymbol{\kappa}\} \end{Bmatrix} - \begin{Bmatrix} \{\mathbf{N}^{\mathrm{T}}\} \\ \{\mathbf{M}^{\mathrm{T}}\} \end{Bmatrix}. \tag{A.15}$$

Appendix B. Material Properties Identification

Elastic Modulus, Coefficient of Thermal Expansion and Density. The principal elastic moduli E_i, the principal CTE α_i, and the density ρ of the materials were measured using the method described in [69]. The results are shown in Tab. 3. The temperature dependence of the principal elastic modulus E_i was measured in the temperature range from room temperature (22 °C) to the glass-transition temperature (or up to 90 °C if the glass transition was not reached). In Tab. 3 principal elastic moduli E_i at room temperature are listed.

Poissons's Ratio. The Poisson's ratio in the 2nd principal direction, when the material is loaded in the 1st principal direction ν_{12}, was measured according to the ISO 527 standard [108]. Three ISO 527-1/1B specimens, each with a thickness of 4 mm and a width of 10 mm, were used for each material. The specimens were 3D-printed with material deposition along their length to ensure loading in the direction of the 1st principal axis. The resulting Poisson's ratio ν_{12} for each material is provided in Tab. 3.

Relaxation Modulus and Shift-Factor. The relaxation modulus in the appropriate principal direction $E_i(t)$ and the shift-factor a_T for the materials were determined by measuring the force reduction over time under constant deformation at various temperatures. Three rectangular samples with dimensions of $20 \times 20 \times 40$ mm were used for each material. Depending on the material being tested, the rectangular samples were 3D-printed with material deposition matching the direction used for the electrothermal actuators (see Sec. 4.1). This allowed the identification of the relaxation modulus in the

1st principal direction for M2 and M3 materials, and in the 2nd principal direction for M1 materials (see Tab. 2).

Fig. B.10 shows the experimental setup for measuring the relaxation modulus. A bench vise was used to apply a precise step deformation to the rectangular sample. The sample was placed between two aluminum blocks in the jaws to ensure uniform contact between the sample and the jaw, as well as between the sample and the load cell. The FX293X-100A-0025-L (TE Connectivity, Switzerland) load cell, positioned between one jaw and the aluminum block and connected to a NI-9215 (National Instruments, USA) measurement card, was used to acquire the compression force. The LK-G82 (Keyence International, Belgium) laser displacement sensor, also connected to the NI-9215, monitored the jaw displacement. The temperature of the rectangular sample was measured using a type K thermocouple and a NI-9211. The experiment was conducted in a 3D printer with an actively temperature-controlled chamber, allowing relaxation measurements at elevated temperatures.

First, the relaxation modulus at room temperature ($T = 22\,^\circ\mathrm{C}$) was measured. After placing the rectangular sample in the jaws, a $1\,\mathrm{N}$ compression force was applied using the vise to hold the system in place. This state was defined as the initial zero-deformation state. A step deformation d_0 was then applied to the sample by the vise, resulting in a compression force of $100\,\mathrm{N}$, and the force $F(t)$ was recorded for $2\,\mathrm{h}$.

Second, relaxation measurements at $30\,^\circ\mathrm{C}$ and $40\,^\circ\mathrm{C}$ were conducted using the actively temperature-controlled chamber of a 3D-printer. The rectangular sample was left at each temperature for $2\,\mathrm{h}$ to heat up to the target

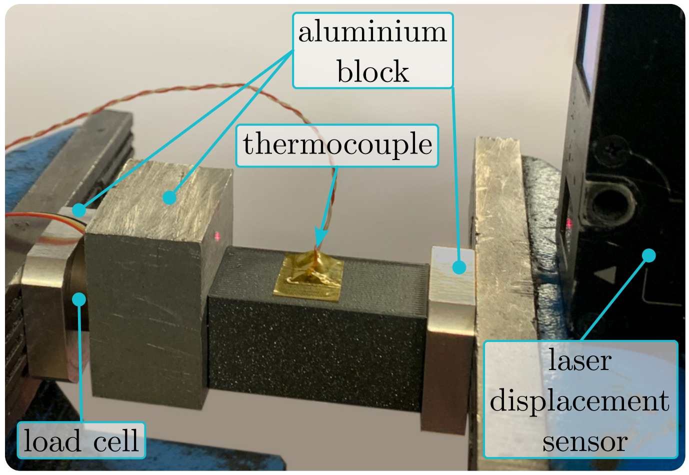

Figure B.10: Experimental setup for measuring the relaxation modulus of 3D-printed rectangular samples. A load cell records the compressive force, and a laser displacement sensor tracks the step deformation. A thermocouple positioned on the sample monitors temperature, while aluminum blocks ensure uniform contact with the compression jaws.

temperature T_{sample} measured by a thermocouple. A 1 N compression force was again applied to establish the initial state. The same step deformation d_0 as used at room temperature was then applied to the sample, resulting in a different final compression force due to the decrease in elastic modulus at elevated temperatures, and the force $F(t)$ was recorded for 2 h.

To obtain the relaxation modulus Eq. (12) was used. The stress $\sigma(t)$ was determined from the measured force $F(t)$ and the cross-sectional area of the rectangular sample A as [96]:

$$\sigma(t) = \frac{F(t)}{A} = \frac{F(t)}{20 \times 20\,\text{mm}}. \tag{B.1}$$

The strain ε_0 was determined using the initial length of the sample L_0 and the applied deformation by the vise d_0 as:

$$\varepsilon_0 = \frac{d_0}{L_0} = \frac{d_0}{40\,\text{mm}}. \tag{B.2}$$

The measured relaxation modulus at room temperature was then approximated by a Prony series with 3 terms, as defined in Eq. (13), using a least squares algorithm to find the optimal values for the relative relaxation terms r_k and characteristic times τ_k [109], which are shown in Tab. 3.

To obtain the shift-factor a_T a least squares algorithm was used to determine the value by which the time t of the relaxation modulus at T_{sample} needs to be scaled (Eq. (15)) to overlap with the relaxation modulus at room temperature on a $\log E(t)$ vs. $\log t$ graph, forming a master curve with $T_{\text{ref}} = 22\,^\circ\text{C}$ [110]. Based on the determined shift-factor values at $T_{\text{sample}} = 30\,^\circ\text{C}$ and $T_{\text{sample}} = 40\,^\circ\text{C}$, the coefficients C_1 and C_2 of the WLF equation (16) were determined. The resulting WLF equation coefficients are shown in Tab. 3.

Electrical resistivity. The electrical resistivity ρ_e of condPLA and condTPU was measured in the direction of the 1st principal axis. Fig. B.11a shows a rectangular sample used for the resistivity measurement. A total of 8 rectangular samples per material were 3D-printed with varying dimensions: length 50 mm and 100 mm, width 10 mm and 20 mm, and thickness 1 mm and 2 mm. The rectangular samples were 3D-printed with material deposition along the x-axis direction, as indicated by the blue line in Fig. B.11a. For the middle 3D-printed layer, an electrically conductive adhesive tape was bonded to the opposite edges of the previously printed layer, overlapping by approximately 3 mm. The next 3D-printed layer was then printed over the conductive tape, creating a solid electrical contact surface, as shown in Fig B.11a.

Once the rectangular samples were 3D-printed, the electrical resistivity

(a)

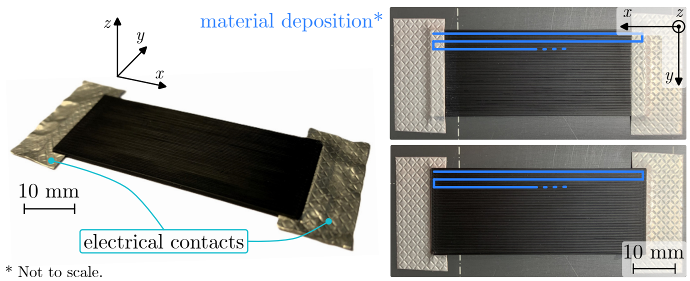

(b)

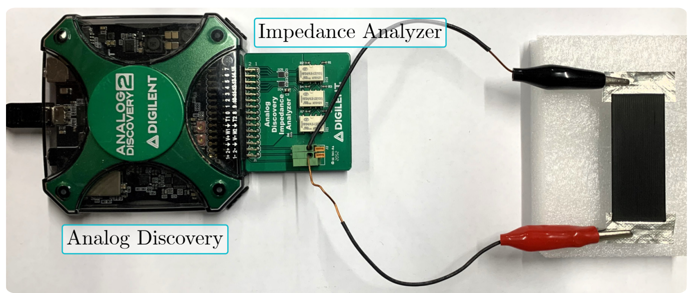

Figure B.11: (a) Rectangular 3D-printed sample (dimensions vary) used to measure electrical resistivity, with conductive tape applied at both ends to ensure reliable electrical contacts. (b) Experimental setup for resistance measurements, with an impedance analyzer connected to the sample via crocodile clips under a constant DC voltage.

ρ_e was determined using Eq. (4). First, the resistance R of the rectangular sample was measured using the experimental setup shown in Fig. B.11b. A Digilent Analog Discovery 2 oscilloscope (Digilent Inc., USA) with an impedance measurement module was used to measure the resistance R of the rectangular sample. The module allowed for DC resistance measurements with calibrated shunt resistors and compensation for the connecting cables. Crocodile clips were attached to the conductive tape for electrical contact. A constant voltage of $3\,\mathrm{V}$ and a $1\,\mathrm{k\Omega}$ shunt resistor were used for the resistance R measurements of the rectangular samples.

Second, the cross-sectional area A of the rectangular sample was determined based on the nominal width and height of the rectangular sample: $A = \text{width} \cdot \text{height}$. For the length of the resistor l, the nominal length of the rectangular sample, shortened by the length of the electrical contact overlap ($2 \cdot 3\,\text{mm}$), was used, since the resistance of the conductive tape is significantly lower compared to the conductive polymer: $l = \text{length} - 6\,\text{mm}$. Using this method, the electrical resistivity was determined for all 8 samples, and the resulting average resistivity is shown in Tab. 3.

Thermal Conductivity and Specific Heat at Constant Pressure. The thermal conductivity k and specific heat C_p of the materials used were measured based on their thermal response. Considering the 3D-printing orientation of the electrothermal actuator, the thermal model requires the value of the thermal conductivity k in the direction of the 3rd principal axis. Fig. B.12a shows a rectangular sample used to measure the thermal conductivity k and specific heat C_p. The rectangular sample has a length of 60 mm, a width of 20 mm, and a height of 3 mm, with a square 3×3 mm hole with a depth of 1 mm in the center of the top surface. The rectangular sample has a sandwich structure consisting of three 1 mm-thick material layers. The bottom and top material layers are made of M1 or M3 material (marked green in Fig. B.12a), while the middle layer consists of the electrically conductive material M2 (marked red in Fig. B.12a). The same combination of conductive and non-conductive materials used for the actuators (Tab. 2) was applied. The thermal conductivity k and specific heat C_p of the M1 or M3 material were measured, with the M2 layer used for heating.

The rectangular samples were 3D-printed with the settings shown in

Tab. 1, stacking the layers in the z direction. The M2 material layer was 3D-printed with material deposited in the x direction. For the non-conductive material layers, the material was deposited in the x direction if M3 material was used, or in the y direction if M1 material was used, to remain consistent with the 3D-printed actuators (see Tab. 2). For electrical contact, electrically conductive tape was used, similar to the setup for the electrical resistivity samples.

Fig. B.12b shows the experimental setup for measuring the thermal conductivity k and specific heat C_p. Initially, the electrical resistance R_h of the rectangular sample was measured using the same method as for electrical resistivity measurements. The rectangular sample was then freely suspended on two ropes, with crocodile clips used for electrical contact on the conductive tape to connect the sample to the DPPS-60-10 (Voltcraft, Germany) voltage generator. A FLIR A50 (Flir, USA) thermal camera was used to measure the temperature on the top surface of the rectangular sample. A step voltage of 60 V was applied to samples with condTPU, and 30 V was applied to samples with condPLA for M2. The average temperature on the surface, in an area 1 mm away from the sample edges, the hole edges, and the ropes (to exclude boundary effects), as well as the average temperature inside the hole, were recorded for 15 min to allow the system to reach steady state. The measurements were performed using 3 rectangular samples for each material.

Initially, the thermal conductivity k and specific heat C_p of condTPU and condPLA were determined. All three material layers of the rectangular samples (M2 and M1/M3) were printed with the same conductive material.

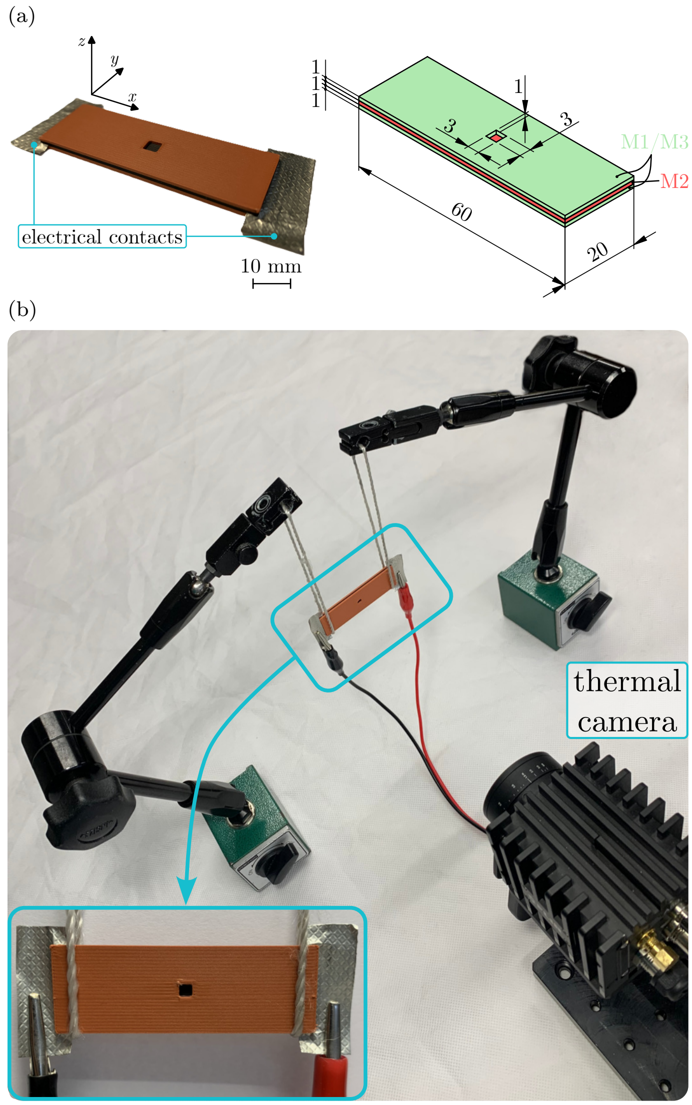

Figure B.12: (a) Rectangular, three-layer sample used for thermal conductivity and specific heat measurements, featuring a small central cavity to monitor temperature distribution. (b) Experimental setup in which the sample is suspended by two ropes and heated via a step voltage, while a thermal camera records surface temperatures for both transient and steady-state analyses.

The thermal conductivity k and specific heat C_p were then determined from the measured surface and hole temperatures by adjusting the material properties in the thermal model to match the measured thermal response. The same thermal model used for the actuators (described in Sec. 3.2) was applied, with 16 nodes, a single material layer, internal heat generation, and convection boundary conditions. For the energy generation rate $\dot{q}$, the applied voltage U, the measured resistance R_h, and the volume of the entire rectangular sample ($V = 60 \times 20 \times 3\,\text{mm}$) were used. The convection boundary condition was applied to both boundary surfaces, with a convection heat transfer coefficient of $h = 12\,\text{W}\,\text{m}^{-2}\,\text{K}^{-1}$ [104] and an ambient air temperature of 22 °C. A least squares algorithm was used to minimize the error between the measured surface and hole temperatures and the temperatures predicted by the thermal model by updating the thermal conductivity k and specific heat C_p. The thermal conductivity k was first determined from the steady-state temperatures, and the specific heat C_p was then determined from the transient part of the measured response. The resulting thermal conductivity k and specific heat C_p of the conductive materials are shown in Tab. 3.

Finally, with the known thermal properties of the conductive materials, the thermal conductivity k and specific heat C_p for the non-conductive materials were determined using the three-layer rectangular sample. The thermal model described in Sec. 3.2, with 6 nodes in each material layer, was used. For the energy generation rate $\dot{q}$, the applied voltage U, the measured resistance R_h, and the volume of only the M2 material layer ($V = 60 \times 20 \times 1\,\text{mm}$) were considered. The convection boundary condition was applied to both boundary surfaces, with a convection heat transfer coefficient of $h = 12\,\mathrm{W\,m^{-2}\,K^{-1}}$ [104] and an ambient air temperature of $22\,°\mathrm{C}$. The same approach as before was used to update the material properties to match the model's predictions with the measured temperatures; however, this time, only the material properties of the outer material layers were updated to obtain the thermal conductivity k and specific heat C_p for the non-conductive materials listed in Tab. 3.